

Low-energy Mott-Hubbard excitations in LaMnO₃ probed by optical ellipsometry

N. N. Kovaleva,^{1,2} Andrzej M. Oleś,^{1,3} A. M. Balbashov,⁴
A. Maljuk,⁵ D. N. Argyriou,⁵ G. Khaliullin,¹ and B. Keimer¹

¹Max-Planck-Institut für Festkörperforschung, Heisenbergstrasse 1, D-70569 Stuttgart, Germany

²Department of Physics, Loughborough University, Loughborough, LE11 3TU, UK

³Marian Smoluchowski Institute of Physics, Jagellonian University, Reymonta 4, PL-30059 Kraków, Poland

⁴Moscow Power Engineering Institute, 105835 Moscow, Russia

⁵Helmholtz-Zentrum Berlin für Materialien und Energie, Glienicker Str. 100, D-14109 Berlin, Germany

(Dated: July 3, 2018)

We present a comprehensive ellipsometric study of an untwinned, nearly stoichiometric LaMnO₃ crystal in the spectral range 1.2–6.0 eV at temperatures 20 K ≤ T ≤ 300 K. The complex dielectric response along the b and c axes of the $Pbnm$ orthorhombic unit cell, $\tilde{\epsilon}^b(\nu)$ and $\tilde{\epsilon}^c(\nu)$, is highly anisotropic over the spectral range covered in the experiment. The difference between $\tilde{\epsilon}^b(\nu)$ and $\tilde{\epsilon}^c(\nu)$ increases with decreasing temperature, and the gradual evolution observed in the paramagnetic state is strongly enhanced by the onset of A -type antiferromagnetic long-range order at $T_N = 139.6$ K. In addition to the temperature changes in the lowest-energy gap excitation at ~ 2 eV, there are opposite changes observed at higher energy at $\sim 4 - 5$ eV, appearing on a broad-band background due to the strongly dipole-allowed O $2p - \text{Mn } 3d$ transition around the charge-transfer energy 4.7 eV. We used a classical dispersion analysis to quantitatively determine the temperature-dependent optical spectral weights shifts between the low- and high-energy optical bands. Based on the observation of a pronounced spectral-weight transfer between both features upon magnetic ordering, they are assigned to high-spin and low-spin intersite $d^4d^4 \rightleftharpoons d^3d^5$ transitions by Mn electrons. The anisotropy of the lowest-energy optical band and the spectral weight shifts induced by antiferromagnetic spin correlations are quantitatively described by an effective spin-orbital superexchange model. An analysis of the multiplet structure of the intersite transitions by Mn e_g electrons allowed us to estimate the effective intra-atomic Coulomb interaction, the Hund exchange coupling, and the Jahn-Teller splitting energy between e_g orbitals in LaMnO₃. This study identifies the lowest-energy optical transition at ~ 2 eV as an intersite $d - d$ transition, whose energy is substantially reduced compared to that obtained from the bare intra-atomic Coulomb interaction.

PACS numbers: 75.47.Lx, 75.30.Et, 78.20.-e

I. INTRODUCTION

LaMnO₃ is the progenitor of a family of manganese oxides that exhibit a multitude of electronic phases and unusual electronic properties such as “colossal” magnetoresistance. The compound crystallizes in the orthorhombically distorted perovskite structure (space group $Pbmn$), in which every Mn ion (with valence state 3+ and high-spin configuration $t_{2g}^3e_g^1$) is surrounded by an octahedron of six oxygen ligands. It is well recognized that a strong Jahn-Teller (JT) instability of the singly occupied e_g orbitals (d_{z^2} and $d_{x^2-y^2}$) gives rise to cooperative distortions of the oxygen octahedra, which induce orbital ordering at $T_{OO} \sim 780$ K^{1,2} and may be responsible for the insulating behavior of LaMnO₃.³ Below $T_N \sim 140$ K, the Mn spins exhibit A -type antiferromagnetic order (*i.e.*, ferromagnetic layers in the ab plane of the orthorhombic lattice, which are antiferromagnetically stacked along the c -axis). In addition to the JT interactions, the phase behavior of LaMnO₃ is determined by superexchange (SE) interactions, which are mediated by $d^4d^4 \rightleftharpoons d^3d^5$ charge excitations along a bond $\langle ij \rangle$ between Mn³⁺ ions and involve both spin and orbital degrees of freedom.^{4,5,6,7} While the magnetic order is stabilized by superexchange, the origin of orbital order in LaMnO₃ is a more subtle issue. Currently, one

of the most intriguing questions in the field of orbital physics of manganites is the role of superexchange interactions (whose magnitude is determined by the on-site Coulomb repulsion U of the Mn d electrons) in the onset of the orbital order and their interplay with the JT electron-phonon interactions.^{3,5,6,7,8,9,10,11} Depending on the value of U , the insulating gap is either of charge-transfer (CT) type (*i.e.*, the chemical potential is between the O $2p$ band and the Mn e_g band), or of Mott-Hubbard type (*i.e.*, the chemical potential is in a gap within the Mn e_g manifold generated by electron-electron and JT electron-phonon interactions).^{10,11,12,13,14,15,16} The corresponding optical transitions across the gap are then either $p - d$ or $d - d$ transitions. A comprehensive description of the nature of the insulating gap and the low-energy optical excitations in LaMnO₃^{17,18,19} is important as a starting point for models of the unconventional phenomena that develop under hole doping, such as colossal magnetoresistance.⁹

Orbital and magnetic ordering phenomena in transition metal oxides are associated with the emergence of anisotropy in the orbital and spin degrees of freedom, and can induce pronounced rearrangements of the optical spectral weight (SW) near the critical temperatures.^{11,17,18,19,20,21,22,23} Therefore the polarization and temperature dependencies of the optical SW can

be instrumental in elucidating the nature of the mechanisms underlying these phenomena.^{6,10,24} The optical SW of the intersite $d-d$ transitions, which is determined by SE interactions, is very sensitive to the temperature-dependent spin correlations, because the spin alignment controls the transfer of electrons between neighboring Mn sites via the Pauli principle. These transitions can thus be singled out by monitoring the evolution of the optical response through the onset of the magnetic order. In contrast to the intersite $d-d$ transitions, the $p-d$ transitions and the on-site $d-d$ transitions should not be affected by the correlations between neighboring Mn spins. The main body of the optical data for insulating LaMnO₃ has been obtained from reflectivity measurements on twinned single crystals. Contrary to theoretical predictions,¹⁰ critical SW shifts at the Néel temperature were not clearly resolved in these experiments.^{17,18}

Following up on a short report,¹⁹ we present here the results of a comprehensive set of spectral ellipsometry experiments in which the complex dielectric function of a nearly stoichiometric, untwinned LaMnO₃ crystal in the spectral range 1.2–5.6 eV was accurately monitored as a function of temperature in the range $20 \text{ K} \leq T \leq 300 \text{ K}$. The dielectric response, $\tilde{\epsilon}^b(\nu)$ and $\tilde{\epsilon}^c(\nu)$, along the b and c axes (*i.e.*, along and perpendicular to the ferromagnetic ab plane) was found to be highly anisotropic, confirming thereby that our crystal is detwinned to a substantial degree. In addition to the anisotropic temperature dependence of the lowest-energy optical band at $\sim 2 \text{ eV}$,¹⁷ strongly temperature dependent optical bands are also observed in the range $\sim 4\text{--}5 \text{ eV}$, appearing on a broad background due to the strongly dipole-allowed O $2p - \text{Mn } 3d$ transition at the $p-d$ charge-transfer energy $\Delta \simeq 4.7 \text{ eV}$. Based on a marked redistribution of the optical SW observed below the Néel temperature, these bands can be assigned to intersite $d^4d^4 \rightleftharpoons d^3d^5$ transitions. Inspection of the spin-dependent selection rules in the magnetically ordered state then yields an assignment of the low- and high-energy $d-d$ bands to transitions into the high-spin (HS, $S = 5/2$) and low-spin (LS, $S = 3/2$) configurations of the Mn²⁺ (d^5) ion, respectively. A self-consistent dispersion analysis of the complex dielectric function enables a reliable separation of the temperature-dependent low- and high-energy counterparts and an estimation their optical SWs.

We also report a detailed quantitative analysis, based on an effective superexchange model, of the optical SW transfer between the HS and LS optical bands induced by antiferromagnetic spin correlations. From the anisotropic temperature behavior of the low-energy HS optical band we estimate the effective “orbital angle” of e_g orbitals resulting from the lattice driven JT effect and the spin-orbital SE interactions. The value of the orbital angle, $\theta = 108^\circ$, established independently in a prior structural study²⁵ is within the limits of our estimate in the framework of the effective superexchange model in the present study. This strongly supports our assignment of the lowest-energy band around 2 eV to the HS intersite

$d-d$ transition. We also analyze the multiplet structure of the LS intersite $d-d$ transitions and find a consistent interpretation of the optical spectra using their assignments. Our analysis implies that LaMnO₃ is in the regime of a Mott-Hubbard rather than CT insulator according to the original classification of Zaanen, Sawatzky and Allen.¹²

The paper is organized as follows. We present details of the experimental studies and sample preparation in Sec. II. In Sec. III A we describe the analysis of the ellipsometry data and present the optical SWs obtained from the dispersion analysis for the two nonequivalent crystallographic directions. The observed anisotropy and temperature dependence of the optical SWs are interpreted using the superexchange model in Sec. III B. Implications for the SE parameters in the context of prior neutron scattering data are discussed in Sec. III C. Sec. IV contains a summary of the main conclusion and a discussion of some open questions.

II. EXPERIMENTAL DETAILS

A. Crystal growth and characterization — sample detwinning

Single crystals of LaMnO₃ were grown by the crucible-free floating zone method using an image furnace equipped with an arc-lamp²⁶ and a four-mirror type image furnace (CSI, Japan) equipped with halogen lamps. The as-grown crystals were characterized by energy dispersive x-ray analysis, x-ray diffraction, and magnetic susceptibility measurements. The as-grown LaMnO₃ single crystals are phase-pure and exhibit the orthorhombic $Pbnm$ structure at room temperature.

In the $Pbnm$ structure, the c -axis direction can be associated with any of the $\langle 100 \rangle$, $\langle 010 \rangle$, and $\langle 001 \rangle$ directions of the high-temperature pseudocubic perovskite $Pm\bar{3}m$ phase. Provided the a and b axes are arbitrarily chosen in the diagonal directions of the perpendicular plane (see Fig. 1(a)), up to six types of orientational domains can exist below the orbital ordering temperature, $T_{OO} \approx 780 \text{ K}$. Therefore, as-grown single crystals of LaMnO₃ always exhibit heavily twinned domain structures. The particular pattern and the sizes of the domains depend on local temperature gradients and mechanical stresses during the growth procedure.

We were able to remove the twins in the essential volume fraction of our sample following the procedure described below. The as-grown single crystal,²⁶ with the orthorhombic c axis coaxial with the axis of growth, was first aligned using x-ray Laue patterns, assuming tentatively the cubic perovskite structure. Then, a slice of thickness $\sim 2 \text{ mm}$ was cut parallel to the plane formed by the orthorhombic c axis and the cubic $\langle 110 \rangle$ direction. From this slice we cut out our sample with dimensions $\sim 3 \times 3 \text{ mm}^2$. Removal of the twins was carried out by heating the sample above $T_{OO} \approx 780 \text{ K}$ under normal

atmosphere conditions, without applying external stress, and subsequent cooling down to room temperature. The domain pattern was visually controlled *in situ* by using a high-temperature optical microscope with crossed optical polarizers. The room temperature polarized optical image of a part of the crystal of 200 μm length showed initially heavily twinned structure of the LaMnO_3 sample (with an average domain width of 5 μm), where four types of different contrasts could be distinguishable (see Fig. 1(c)). On heating the sample the polarized optical images showed decreased color contrast, and close to the temperature of T_{OO} , most of the crystal surface acquired a bright uniform color, and the twinned structure suddenly disappeared. Subsequent cooling down to room temperature was carried out under *in situ* control, with manually optimized parameters. A polarized image of the same part of the crystal after cooling down to room temperature is shown in Fig. 1(d). One can notice that the fine domain structure still persisted in the sample.

The orthorhombic a direction was identified perpendicular to the crystal surface by single-crystal x-ray diffraction analysis. This analysis also confirmed that the crystal was essentially detwinned: at some points of the crystal surface the percentage of detwinning was as high as 95 % (as follows from the Laue diagram shown in Fig. 1(b)), and over the entire surface it was not worse than 80 %. The sample was further characterized by magnetometry, using a superconducting quantum interference device. We determine the antiferromagnetic transition temperature at $T_N \simeq 139.6$ K, which is characteristic for a nearly oxygen-stoichiometric LaMnO_3 crystal.

B. Ellipsometry technique

The technique of ellipsometry provides significant advantages over conventional reflection methods in that (i) it is self-normalizing and does not require reference measurements and (ii) $\varepsilon_1(\nu)$ and $\varepsilon_2(\nu)$ are obtained directly without a Kramers-Kronig transformation. The measurements in the frequency range of 4000-48000 cm^{-1} (0.5-6.0 eV) were performed with a home-built ellipsometer of rotating-analyzer type,²⁷ where the angle of incidence is 70.0°. For optical measurements the surfaces were polished to optical grade. The sample was mounted on the cold finger of a helium flow UHV cryostat in which the temperature could be varied between 10 and 300 K. To avoid contamination of the sample surface with ice, we evacuated the cryostat to a base pressure of about 5×10^{-9} Torr at room temperature. With only a single angle of incidence, the raw experimental data are represented by real values of the ellipsometric angles, Ψ and Δ , for any wave number. These values are defined through the complex Fresnel reflection coefficients for light polarized parallel (r_p) and perpendicular (r_s) to the plane of incidence

$$\tan \Psi e^{i\Delta} = \frac{r_p}{r_s}. \quad (1)$$

To determine the complex dielectric response $\tilde{\varepsilon}_b(\omega)$ and $\tilde{\varepsilon}_c(\omega)$ of the LaMnO_3 crystal, we have measured ellipsometric spectra with b or c axes aligned perpendicular to the plane of incidence of the light, respectively. In the following, we present the complex dielectric response $\tilde{\varepsilon}(\omega)$ extracted from the raw ellipsometry spectra, $\Psi(\omega)$ and $\Delta(\omega)$.

III. RESULTS AND DISCUSSION

A. Anisotropic dielectric response and spectral weight

1. Overall description and temperature dependencies

Figures 2 and 3 show temperature dependencies of the real and imaginary parts of the dielectric function, $\tilde{\varepsilon}(\nu) = \varepsilon_1(\nu) + i\varepsilon_2(\nu)$, in b -axis and c -axis polarization, respectively, extracted from our ellipsometric data. One can notice strong anisotropy in the complex dielectric function spectra, $\tilde{\varepsilon}^b$ and $\tilde{\varepsilon}^c$. The anisotropy in the optical spectra appears in the orbitally-ordered state below $T_{OO} \simeq 780$ K.¹⁷ The strong optical anisotropy of our spectra thus confirms that our crystal has been detwinned to a substantial degree.

From Figs. 2 and 3 one can see that the spectra ε_2^b and ε_2^c are dominated by two broad optical bands: at low energies around 2 eV and at high energies around 5 eV. Superimposed are a number of smaller spectral features. In particular, one can clearly see in the room temperature ε_2^b spectrum that the low-energy optical band consists of three distinct bands that are reliably resolved owing to the accuracy of the ellipsometric data. At room temperature, the anisotropy is most pronounced in the low-energy optical band around 2 eV. This band is noticeably suppressed in c -axis polarization. With decreasing temperature, the anisotropy between $\tilde{\varepsilon}^b$ and $\tilde{\varepsilon}^c$ increases and becomes strongly enhanced below $T_N \simeq 140$ K.

Figures 4 and 5 display the evolution of the difference between the low-temperature complex dielectric function spectra measured at 20 K and the corresponding T -dependent spectra, $\Delta\tilde{\varepsilon}(20\text{K}, T) = \tilde{\varepsilon}(20\text{K}) - \tilde{\varepsilon}(T)$, in the b -axis and c -axis polarization, respectively. In accordance with the earlier optical study on a detwinned LaMnO_3 crystal by Tobe *et al.*,¹⁷ these data clearly demonstrate opposite trends in the temperature behavior of the low-energy optical band around 2 eV in the b -axis and c -axis polarization. However, our present ellipsometry study in an extended spectral range up to 6 eV shows that there are obvious counterparts for the low-energy changes in the b -axis and c -axis polarization, appearing at higher energies. Further, by using a classical dispersion analysis of the T -dependent dielectric function spectra, we determine more accurately which optical bands are involved in the process of the spectral redistribution.

2. Spectral weight shifts: partial low- and high-energy components

Analyzing the data shown in Figs. 4 and 5, we estimate the associated SW changes, $\Delta SW(\nu_0, \nu) = 1/(4\pi) \int_{\nu_0}^{\nu} \nu' \Delta \varepsilon_2(\nu') d\nu' = \int_{\nu_0}^{\nu} \Delta \sigma_1(\nu') d\nu'$, and follow their evolution with temperature. These data are presented in Figs. 6(a) and (b) for the b -axis and c -axis polarization, respectively, expressed in terms of the effective number of charge carriers, $\Delta N_{eff} = \frac{2m}{\pi e^2 N} \Delta SW$, where m and e are the free-electron mass and charge, and $N = a_0^{-3} = 1.7 \times 10^{22} \text{ cm}^{-3}$ is the density of Mn atoms. One can notice from Fig. 6(a) that the b -axis low-energy SW increases upon cooling. This trend persists up to ~ 2.7 eV and can be associated with a SW *gain* of the low-energy optical band around 2 eV with decreasing temperature. At higher energies, we observe a corresponding SW *loss*. As shown in Fig. 6(b), the opposite trend holds for the c -axis SW changes, however, the low-energy SW decreases here up to 3.8 eV. We evaluate the SW changes associated with the high-energy optical bands as an amplitude value between the onset of the contribution from the high-energy optical bands and the high-energy limits, where the SW changes are nearly saturated, as explicitly indicated in Figs. 6(a) and (b). In Fig. 7(a) and (b) we plot the temperature dependencies of these SW changes, which can be associated with the *partial SW gain* or *loss* of the low-energy and high-energy optical bands in the b -axis and c -axis polarization, respectively. This estimates the *partial SW shifts* between the low- and high- energy optical bands. The temperature-dependent profiles exhibit clear kinks around the magnetic ordering temperature $T_N \simeq 140$ K, which highlights the influence of spin correlations on the SW shifts in the anisotropic dielectric response of LaMnO₃.

3. Evaluation of total spectral weight

To separate contributions from the low- and high-energy optical bands and estimate the associated *total SWs*, we performed a classical dispersion analysis. Using a dielectric function of the form $\tilde{\varepsilon}(\nu) = \epsilon_{\infty} + \sum_j \frac{S_j \nu_j^2}{\nu_j^2 - \nu^2 - i\nu\gamma_j}$, where ν_j , γ_j , and S_j are the peak energy, width, and dimensionless oscillator strength of the j th oscillator, and ϵ_{∞} is the core contribution from the dielectric function, we fit a set of Lorentzian oscillators simultaneously to $\varepsilon_1(\nu)$ and $\varepsilon_2(\nu)$. To obtain an accurate description of the anisotropic complex dielectric functions, $\tilde{\varepsilon}^b(\nu)$ and $\tilde{\varepsilon}^c(\nu)$, which are presented in Figs. 2 and 3, we need to introduce a minimum set of six oscillators: three for the low-energy three-band feature, and three more for the high-energy optical features which can be recognized by the imaginary resonance part and the corresponding real antiresonance part at around 4, 4.5-5 eV, and near 6 eV. In our analysis we assume that the SW

of the optical bands above the investigated energy range remains T -independent. For the sake of definiteness we introduce only one high-energy optical band peaking at 8.7 eV, with the parameters $S = 1.87$ and $\gamma = 5.0$ eV that have been estimated from the reflectivity study on a twinned LaMnO₃ crystal by Arima *et al.*¹³ Figures 8 and 9 summarize the results of our dispersion analysis of the complex dielectric response at 20 and 300 K in the b -axis and c -axis polarization, respectively. One can notice from the figures that the constituent optical bands from the low- and high-energy sides are strongly superimposed, and therefore cannot be unequivocally separated. The corresponding T -dependencies of the peak energies ν_j of the optical bands in ε_2^b and ε_2^c are detailed in Fig. 10. To check the robustness of our fit, we have performed the dispersion analysis on two data sets generated by cycling the temperature from 20 to 300 K and from 300 to 20 K. As one can notice from this figure, the accuracy in the determination of the peak energy of the optical band at around 6 eV is limited, which can be naturally explained by the uncertainties at higher energies, beyond the investigated spectral range. However, the fit is quite robust at low energies, so that the peak energies of the constituent optical bands can be accurately determined.

For an individual Lorentz oscillator the associated SW can be estimated as $SW = \frac{\pi}{120} S_j \nu_j^2$. We evaluate the *total SW* of the low-energy optical band as the sum of the contributions of the three separate Lorentz oscillators peaking at low temperatures at around 2.0 ± 0.1 eV, 2.4 ± 0.1 eV, and 2.7 ± 0.1 eV. The T -dependencies of the *total SW* of the low-energy optical band in the b -axis and c -axis polarization are shown in Fig. 11. One can see that the *total SW* of the low-energy optical band at around 2 eV shows pronounced changes over the entire investigated temperature range in the b -axis response, with a discernible kink near $T_N \simeq 140$ K, while the corresponding changes along the c -axis are strongly suppressed.

In contrast to the low-energy optical bands, their T -dependent counterparts at high energies appear on a background of a strongly pronounced optical band at ~ 4.7 eV. Based on a comparison to optical data on other transition metal oxides and to a variety of theoretical calculations,^{13,28,29} this band can be assigned to the strongly dipole-allowed $p-d$ transition. The high-energy optical bands experiencing changes around T_N appear in the spectra above 3 eV, and among them we are able to distinguish the optical bands peaking at low temperatures at around 3.9 ± 0.1 eV, 4.4 ± 0.1 eV, 4.8 ± 0.1 eV, and 5.7 ± 0.5 eV. Using the results of the present dispersion analysis, we evaluate the T -dependent shifts of the *total SW* of the high-energy optical bands as $\Delta SW(0, 6eV) = 1/(4\pi) \int_0^{6eV} \nu' \Delta \varepsilon_2(\nu') d\nu'$.

B. Fingerprints of spin-orbital superexchange interactions in the low-energy optical response

1. Multiplet structure

Superexchange interactions between Mn^{3+} ions originate from various charge excitations $d_i^4 d_j^4 \rightleftharpoons d_i^5 d_j^3$, which arise from a transition of either a e_g or a t_{2g} single electron between two ions, leading to different excited states at the resulting Mn^{2+} (d^5) ion. Here we use an effective model⁵ for the superexchange between Mn^{3+} ions, where all the excitation processes going via intermediate oxygen $O(2p_\sigma)$ orbitals are absorbed in the effective hopping element t which plays the role of an effective ($dd\sigma$) hopping element.¹⁴

In order to parameterize the intersite $d_i - d_j$ optical excitations we introduce the following two parameters: an effective Coulomb element U and Hund's exchange between two e_g electrons J_H , see e.g. Ref. 6. While J_H is only a somewhat screened atomic value, the parameter U is not simply a single-ion property but should include both the renormalization by the nearest-neighbor Coulomb interaction V , and the polarization contribution P .³⁰ Therefore, its relation to the intraorbital Coulomb repulsion U_0 is: $U = U_0 - V - 2zP$, where z is the number of neighbors. Fortunately, the same intersite $d - d$ charge excitations are measured in the optical spectroscopy and determine the superexchange by virtual $d_i^4 d_j^4 \rightleftharpoons d_i^5 d_j^3$ transitions, so a single effective parameter U suffices to describe both the optical SWs and the magnetic exchange constants.^{24,31} Hereafter, the parameter U includes all of these renormalization effects. For e_g electron excitations between two Mn^{3+} ions, $(t_{2g}^3 e_g^1)_i (t_{2g}^3 e_g^1)_j \rightleftharpoons (t_{2g}^3 e_g^2)_i (t_{2g}^3 e_g^0)_j$, the five possible excited states are:³² (i) the high-spin (HS) 6A_1 state ($S = 5/2$), and (ii)-(v) the low-spin (LS) ($S = 3/2$) states 4A_1 , 4E (${}^4E_\varepsilon$, ${}^4E_\theta$) and 4A_2 . The energies of these excited states are given in terms of the Racah parameters in Ref. 32. In order to parameterize this spectrum by J_H , which for a pair of e_g electrons is given by Racah parameters B and C as $J_H = 4B + C$, we apply an approximate relation $4B \simeq C$, justified by the atomic values for a Mn^{2+} (d^5) ion, $B = 0.107$ eV and $C = 0.477$ eV.³³ Then the excitation spectrum simplifies to:^{6,7}

- (i) 6A_1 at the energy $E_1 = U - 3J_H + \Delta_{JT}$,
- (ii) 4A_1 at $E_2 = U + 3J_H/4 + \Delta_{JT}$,
- (iii) ${}^4E_\varepsilon$ at $E_3 = U + 9J_H/4 + \Delta_{JT} - \sqrt{\Delta_{JT}^2 + J_H^2}$,
- (iv) ${}^4E_\theta$ at $E_4 = U + 5J_H/4 + \Delta_{JT}$, and
- (v) 4A_2 at $E_5 = U + 9J_H/4 + \Delta_{JT} + \sqrt{\Delta_{JT}^2 + J_H^2}$.

Here U is the Coulomb repulsion of two electrons with opposite spins occupying the same e_g orbital as introduced above, and Δ_{JT} is the Jahn-Teller splitting of the two e_g levels.

Figures 6, 7, and 11 clearly demonstrate that the optical spectral weight shifts in LaMnO_3 are strongly influenced by the onset of long-range antiferromagnetic order. The local CT excitations between the O $2p$ states and Mn

$3d$ states should not be affected by the relative orientation of neighboring Mn spins. Therefore, the strongly T -dependent bands can be associated with excitations of intersite transitions of the form $d_i^4 d_j^4 \rightleftharpoons d_i^5 d_j^3$. Below the magnetic transition ($T < T_N$), the A -type antiferromagnetic spin alignment favors HS transitions along the bonds in the ferromagnetic ab plane and disfavors them along the c -axis for antiferromagnetically ordered spins, in agreement with the observed SW evolution of the low-energy band at around 2 eV (see Figs. 6 and 11). As reported before¹⁹, the optical transition at $\sim 2.0 \pm 0.1$ eV, which exhibits a SW increase due to FM ordering in the ab plane at low temperatures, can be therefore related to excitations into the HS (6A_1) state, where the valence electron is transferred to an unoccupied e_g orbital on the neighboring Mn site with a parallel spin. The three-subband structure of this band will require more elaborate experimental and theoretical considerations and will be studied elsewhere.

The higher-energy optical bands which exhibit the converse SW evolution below T_N can be then related to the LS-state transitions. Following the temperature variation of the complex dielectric function spectra for c -axis polarization, we clearly resolve the strongly T -dependent optical band at $\sim 4.4 \pm 0.1$ eV (see Figs. 3 and 5), which is involved in the process of the SW transfer between the low- and high-energy bands in the investigated energy range. This high-energy optical band, which exhibits a SW increase in the c -axis polarization upon the A -type spin alignment, can be therefore attributed to LS transitions. This band can be identified with the next-highest energy levels (ii)-(iv), which are nearly degenerate and centered around $\sim U + J_H + \Delta_{JT}$ if $\Delta_{JT} \lesssim J_H$. (Note that this condition is indicated by band structure calculations¹¹ and consistent with our analysis of the optical spectral weight; see below.) The difference between the energies of the lowest-lying LS and HS transitions then implies $J_H = 0.6 \pm 0.1$ eV.³⁴ The analysis presented thus far puts the constraint $U + \Delta_{JT} = E_1 + 3J_H = 3.8$ eV on the remaining parameters U and Δ_{JT} . An analysis of the spectral weight and lineshape of the optical band at 4.4 eV then leads to the following excitation energies: (ii) and (iii) 4.3 ± 0.2 eV, (iv) 4.6 ± 0.2 eV, and (v) 6.1 ± 0.2 eV, which imply $U = 3.1 \pm 0.2$ eV³⁵ and $\Delta_{JT} = 0.7 \pm 0.2$ eV. We defer an explanation of the reasoning behind this assignment and the associated uncertainties to the end of this subsection, after we have presented the theoretical analysis of the optical spectral weights in terms of a superexchange model.

2. Optical spectral weight

The effective SE Hamiltonian for a bond $\langle ij \rangle$ due to the different excitations of e_g electrons (i) – (v) reads:^{5,6,7}

$$H_{ij}^{(\gamma)} = \frac{t^2}{20} \left\{ -\frac{1}{E_1} (\vec{S}_i \cdot \vec{S}_j + 6)(1 - 4\tau_i\tau_j)^{(\gamma)} + \frac{1}{8} \left(\frac{3}{E_2} + \frac{5}{E_4} \right) (\vec{S}_i \cdot \vec{S}_j - 4)(1 - 4\tau_i\tau_j)^{(\gamma)} + \frac{5}{8} \left(\frac{1}{E_3} + \frac{1}{E_5} \right) (\vec{S}_i \cdot \vec{S}_j - 4)(1 - 2\tau_i)^{(\gamma)}(1 - 2\tau_j)^{(\gamma)} \right\}. \quad (2)$$

Here t is the effective $dd\sigma$ electron hopping amplitude, which describes the hopping process along the Mn-O-Mn bond and follows from the CT model.¹⁴ The pseudospin operators $\tau_i^{(\gamma)}$ depend on the orbital state and on the bond direction $\langle ij \rangle \parallel \gamma$, where γ denotes nonequivalent cubic directions – either a or b in the ab plane or c axis. Averages of the orbital projection operators for the C -type orbital ordering of occupied e_g orbitals alternating in the ab plane can be determined⁶ from the orbital order described by the orbital angle θ in the relevant temperature range,³⁶

$$(1 - 4\tau_i\tau_j)^{(ab)} = \left(\frac{3}{4} + \sin^2 \theta \right), \quad (3)$$

$$(1 - 4\tau_i\tau_j)^{(c)} = \sin^2 \theta, \quad (4)$$

$$(1 - 2\tau_i)(1 - 2\tau_j)^{(ab)} = \left(\frac{1}{2} - \cos \theta \right)^2, \quad (5)$$

$$(1 - 2\tau_i)(1 - 2\tau_j)^{(c)} = (1 + \cos \theta)^2. \quad (6)$$

One may associate the kinetic energy $K^{(\gamma)}$ of virtual charge transitions with the SW as $N_{\text{eff}} = (ma_0^2/\hbar^2)K^{(\gamma)}$ for the tight-binding models. As shown in Ref. 24, this SW can be determined from a related term in the SE energy (Eq. (2)) via the optical sum rule

$$K_n^{(\gamma)} = -2\langle H_{ij,n}^{(\gamma)} \rangle, \quad (7)$$

where n is an excitation with energy E_n . First we use Eq. (7) to estimate the SW of the HS (6A_1) excitations and introduce the kinetic energies

$$K_{\text{HS}}^{(ab)} = \frac{1}{10} \frac{t^2}{E_1} \langle \vec{S}_i \cdot \vec{S}_j + 6 \rangle^{(ab)} \left(\frac{3}{4} + \sin^2 \theta \right), \quad (8)$$

$$K_{\text{HS}}^{(c)} = \frac{1}{10} \frac{t^2}{E_1} \langle \vec{S}_i \cdot \vec{S}_j + 6 \rangle^{(c)} \sin^2 \theta. \quad (9)$$

The temperature dependence of the SWs follows from the spin correlation functions. For $T \ll T_N$, $\langle \vec{S}_i \cdot \vec{S}_j \rangle^{(ab)} \rightarrow 4$ and $\langle \vec{S}_i \cdot \vec{S}_j \rangle^{(c)} \rightarrow -4$ within the classical approximation, while $\langle \vec{S}_i \cdot \vec{S}_j \rangle^{(ab,c)} \rightarrow 0$ for $T \gg T_N$. As one can notice from Eqs. (7) and (8) the anisotropy ratio of the low-temperature and high-temperature SW of the HS (6A_1)

excitation is governed by the orbital angle θ . In Fig. 11 we show anisotropic temperature dependencies of the SW of the low-energy optical band at 2 eV, represented by the summary contribution from the three subbands¹⁹, resulting from the dispersion analysis as described above.

Interestingly, the low-energy SW provides a constraint which might serve to estimate the orbital angle θ by solving the equation

$$N_{\text{eff,HS}}^{(ab)}(T \ll T_N) = \frac{5}{3} \left(\frac{3}{4\sin^2 \theta} + 1 \right) N_{\text{eff,HS}}^{(c)}(T \gg T_N), \quad (10)$$

using the experimental values $N_{\text{eff,HS}}^{(ab)}(T \ll T_N) \simeq 0.28 \pm 0.01$ and $N_{\text{eff,HS}}^{(c)}(T \gg T_N) \simeq 0.075 \pm 0.015$. This estimate gives the orbital angle θ in the range $104^\circ \lesssim \theta \lesssim 140^\circ$. We note that θ is actually limited from above by the JT orbital angle of 120° . However, the value of the orbital angle $\theta_s = 108^\circ$, determined from the structural data by Rodríguez-Carvajal *et al.*,²⁵ is within the estimated limits. Using $\theta = 108^\circ$ for definiteness, we evaluate the effective transfer integral $t \simeq 0.41 \pm 0.01$ from the LT limit $N_{\text{eff,HS}}^{(ab)}(T \ll T_N) \simeq 0.28 \pm 0.01$.³⁷ Then, the associated SW variation between the low- and high-temperature limits in ab polarization is $\Delta N_{\text{eff,HS}}^{(ab)} \simeq \frac{2}{10} \frac{t^2}{E_1} 4 \left(\frac{3}{4} + \sin^2 \theta \right) \simeq 0.11 \pm 0.005$, whereas it amounts $\Delta N_{\text{eff,HS}}^{(c)} \simeq \frac{2}{10} \frac{t^2}{E_1} 4 \sin^2 \theta \simeq 0.06 \pm 0.005$ in the c polarization. It is remarkable that the temperature dependencies of the anisotropic ab plane and c axis SW of the HS (6A_1) excitation, calculated with these parameters along the lines of Ref. 6, correctly reproduce the experimental temperature dependencies of the *total* SW of the low-energy optical band at 2 eV (see Fig. 11).

Using the above parameters we now estimate the low-temperature limits and variation of the SW between the low- and high-temperature limits for the combined SW of the LS excitations (ii)–(v) from the SE Hamiltonian given by Eq. (2). Taking the classical value of the spin correlation function $\langle \vec{S}_i \cdot \vec{S}_j \rangle^{(ab)} \rightarrow 4$ for $T \ll T_N$, it follows from Eq. (2) that the low-temperature (LT) limit of the SW of the LS-state optical excitations vanishes in the ferromagnetic ab plane.³⁸ For the high-temperature (HT) limit $T \gg T_N$, $\langle \vec{S}_i \cdot \vec{S}_j \rangle^{(ab)} \rightarrow 0$, and using the corresponding averages for the orbital projection operators in the ab polarization one finds the combined SW $N_{\text{eff,LS}}^{(ab)}(T \gg T_N) \simeq 0.071$ (with the contributions from the individual LS-state excitations (ii) 0.0193, (iii) 0.0128, (iv) 0.0302, and (v) 0.0090). For the LT limit $T \ll T_N$ in the c polarization, $\langle \vec{S}_i \cdot \vec{S}_j \rangle^{(c)} \rightarrow -4$, and one can get an estimate for the combined SW $N_{\text{eff,LS}}^{(c)}(T \ll T_N) \simeq 0.086$ (with the following individual contributions: (ii) 0.0212, (iii) 0.0186, (iv) 0.0331, and (v) 0.0131). Then, the SW variation between the LT and HT limits is $\Delta N_{\text{eff,LS}}^{(c)} \simeq 0.043$ in c -polarization.

A comparison between the theoretical and the experimental temperature-dependent SWs follows from the

suggested assignments for the HS and LS optical bands (Figs. 13 and 14). We separately present the *partial* SW obtained by direct integration of the experimental spectrum between the limits shown in Fig. 6, and the *total* SW resulting from the dispersion analysis described in Section III.A.3 (which includes tails of the constituent optical bands). One can notice from Fig. 13 that the *partial* SW of the 2 eV optical band, in contrast to its *total* SW, does not show clear critical behavior around the Néel temperature T_N in the b -axis polarization. This could be the reason why Tobe *et al.*¹⁷ did not recognize the critical behavior in the temperature dependence of the *partial* SW of the 2 eV optical band around T_N in their study, and as a result concluded that $p-d$ transitions determine the character of this low-energy excitation. As one can notice from 13 and 14, between the low-temperature limit and T_N , the anisotropic temperature dependencies of the experimental *total* SW of the low-energy 2 eV optical band and the high-energy optical bands of LS character are, in general, well reproduced by the *total* SW resulting from the $e_g \rightleftharpoons e_g$ SE Hamiltonian (Eq. (2)). However, in the analysis of the *partial* and *total* anisotropic SW of the LS states, the uncertainties due to the contribution from the high-energy LS-state transition (v) at ~ 6.1 eV and additional contributions from the $t_{2g} \rightleftharpoons t_{2g}$ and $e_g \rightleftharpoons t_{2g}$ transitions, as discussed below, may result in the larger error bars. Moreover, the deviation of the LS-state optical SW above T_N can be attributed to high-temperature anharmonicity effect of the dominating background, represented by the strongly dipole-allowed $p-d$ transition at ~ 4.7 eV.

In the c -axis response we observe the optical band at ~ 3.8 eV, which clearly exhibits the HS character, and becomes most pronounced at 300 K, simultaneously with the HS low-energy optical band at 2 eV (see Figs. 3 and 5). Due to the presence of this extra HS-state optical excitation the isosbestic point in the c -axis polarization is shifted to the higher energy, and, therefore, the low-energy SW decreases here until the energy of ~ 3.8 eV, as one can notice from Fig. 6(b). In our previous study,¹⁹ we assigned the band at around 3.8 eV, pronounced in the $\tilde{\varepsilon}^c(\nu)$ and $\Delta\tilde{\varepsilon}^c(\nu)$ (see Figs. 3, 5 and 9), to the inter-site $t_{2g} \rightleftharpoons e_g$ HS-state excitation. In agreement with the assignment of the 2 eV optical band to the $e_g \rightleftharpoons e_g$ HS transition, this transition could be observed at the energies shifted up by the crystal field splitting $10Dq \sim 1.5$ eV. The polarization dependence of the band at ~ 3.8 eV can be then naturally explained by the C -type ordering of the unoccupied e_g orbitals. In the c axis, the SW *loss* between 20 K and 300 K, corresponding to the extra HS contribution of the 3.8 eV optical band in the spectral range between 3 and 3.8 eV, is about ~ 0.02 , as follows from Fig. 6(b). Then, the cumulative SW variation of the 2 and 3.8 eV optical bands between the low- and high-temperature limits in the c -axis polarization will amount to $\Delta N_{\text{eff,HS}}^{(c)} \simeq 0.06 + 0.02 = 0.08$. In the b -axis polarization the SW changes of the 3.8 eV optical band between the low- and high-temperature limits can

be estimated as the missing SW in the balance of the 2 eV HS band and the higher energy LS bands. In accordance with the analysis presented above, this amounts to $0.11 - 0.07 = 0.04$. Then, the cumulative SW variation of the 2 and 3.8 eV optical bands between the low- and high-temperature limits in the b -axis polarization is $\Delta N_{\text{eff,HS}}^{(ab)} \simeq 0.11 + 0.04 = 0.15$ eV.

The calculated temperature variations of the spectral weights of the closely spaced LS excitations (ii) – (iv), in combination with the data of Fig. 5, allow us to put further constraints on the structure of the level spectrum and the model parameter Δ_{JT} (which controls the energy of level (iii) relative to those of (ii) and (iv)). To this end, we have numerically computed the complex dielectric response along the c -axis for different values of Δ_{JT} in the range 0 – 1 eV, using the spectral weights calculated from the SE model. Since the calculated $\Delta N_{\text{eff}}^{(c)}$ of excitation (iv) is approximately twice as large as the ones of excitations (ii) and (iii), the narrow, symmetric lineshape of the 4.4 eV feature in the temperature-difference spectrum $\Delta\varepsilon_2^{(c)}$ in Fig. 5(b) is best reproduced if Δ_{JT} is chosen such that $E_2 \approx E_3$, and this doublet and level E_4 are grouped around the peak energy 4.4 ± 0.1 eV. This is the case for $\Delta_{JT} = 0.7 \pm 0.2$ meV, yielding $E_2 \approx E_3 = 4.3 \pm 0.2$ eV, $E_4 = 4.6 \pm 0.2$ eV, and $E_5 = 6.1 \pm 0.2$ eV. Level (v) is therefore expected to be outside the measured energy range, which explains why it is not observed experimentally. We have verified that asymmetric profiles of $\Delta\varepsilon_2^{(c)}$ inconsistent with our data are generated if Δ_{JT} is chosen outside the quoted uncertainty limits. The constraint $U + \Delta_{JT} = E_1 + 3J_H$ discussed above then yields $U = 3.1 \pm 0.2$ eV for the effective intra-atomic Coulomb repulsion. We emphasize that J_H and the sum $U + \Delta_{JT}$ can be inferred from the positions of the temperature-dependent optical bands at 2 and 4.4 eV alone, whereas the separate determination of U and Δ_{JT} relies on a spectral-weight analysis of three excitations that are not resolved experimentally. The latter determination should thus be regarded as more tentative. However, the main conclusions of our paper do not rely on the numerical values of these parameters.

C. Magnetic exchange constants

Finally, we consider the magnetic exchange constants, J_{ab} and J_c , to verify whether the presented interpretation is consistent also with the magnetic properties of LaMnO_3 . From the effective SE Hamiltonian, Eq. (2), one finds,

$$H_S = J_c \sum_{\langle ij \rangle_c} \vec{S}_i \cdot \vec{S}_j + J_{ab} \sum_{\langle ij \rangle_{ab}} \vec{S}_i \cdot \vec{S}_j, \quad (11)$$

where J_{ab} and J_c are determined by the e_g and t_{2g} contributions as follows^{6,7}

$$J_{ab} = \frac{t^2}{20} \left\{ \left(-\frac{1}{E_1} + \frac{3}{8E_2} + \frac{5}{8E_4} \right) \left(\frac{3}{4} + \sin^2\theta \right) + \frac{5}{8} \left(\frac{1}{E_3} + \frac{1}{E_5} \right) \left(\frac{1}{2} - \cos\theta \right)^2 \right\} + J_t, \quad (12)$$

$$J_c = \frac{t^2}{20} \left\{ \left(-\frac{1}{E_1} + \frac{3}{8E_2} + \frac{5}{8E_4} \right) \sin^2\theta + \frac{5}{8} \left(\frac{1}{E_3} + \frac{1}{E_5} \right) (1 + \cos\theta)^2 \right\} + J_t. \quad (13)$$

Here the e_g part is obtained from the SE Hamiltonian given by Eq. (2) and is anisotropic in the state with orbital order. In contrast, the t_{2g} contribution, represented by J_t , is orbital independent and isotropic. It follows from charge excitations by t_{2g} electrons,⁵ $(t_{2g}^3 e_g^1)_i (t_{2g}^3 e_g^1)_j \rightleftharpoons (t_{2g}^4 e_g^1)_i (t_{2g}^2 e_g^1)_j$ excitations along a bond $\langle ij \rangle$, which involve 4T_1 and 4T_2 configurations at both Mn^{2+} and Mn^{4+} ions. The t_{2g} part of the SE is antiferromagnetic, with the excitation energies (estimated from our parameters $U \simeq 3.1$ eV and $J_H \simeq 0.6$ eV):^{5,6} $\varepsilon({}^4T_1, {}^4T_2) \simeq U + 5J_H/4$ (~ 3.85 eV), $\varepsilon({}^4T_2, {}^4T_2) \simeq U + 9J_H/4$ (~ 4.45 eV), $\varepsilon({}^4T_1, {}^4T_1) \simeq U + 11J_H/4$ (~ 4.75 eV), and $\varepsilon({}^4T_2, {}^4T_1) \simeq U + 15J_H/4$ (~ 5.35 eV). The t_{2g} excitations are all LS ($S = 3/2$) and could be partly superimposed with the LS part of the e_g excitations at the specified energies. While the first three of them might be difficult to separate from the e_g contributions, we do not find any evidence on the highest energy contribution at energy around ~ 5.4 eV which suggests rather low intensity of this excitation. Moreover, the good qualitative agreement between the superexchange e_g model and the *total* optical spectral weight confirms that the leading term in the HS and LS part in the b -axis and c -axis polarization comes from the e_g optical excitations, while the t_{2g} excitations contribute with a relatively small SW. This is also consistent with theoretical expectations according to which the optical spectral weights due to the t_{2g} excitations are proportional to the respective superexchange terms. They arise from processes via $O(2p_\pi)$ orbitals with the hopping t_π , and are therefore lower than those following from e_g excitations by $(t_\pi/t)^2$, i.e. roughly by one order of magnitude; see also Ref. 6. Nevertheless, these excitations provide an important contribution to the magnetic exchange constants as all the terms have the same sign, unlike for the e_g part.

The experimental values of the anisotropic magnetic exchange constants for the A -type antiferromagnetic phase of LaMnO_3 , $J_{ab}^{\text{exp}} = -1.67$ meV and $J_c^{\text{exp}} = 1.2$ meV,³⁹ are reproduced for the orbital angle $\theta = 94^\circ$ when the present effective parameters $\{U, J_H, \Delta_{\text{JT}}\}$ are used to determine the excitation energies $\{E_n\}$ in Eqs. (12) and (13). In Fig. 14 we show the dependencies of both exchange constants, J_{ab} and J_c , on the orbital angle θ , calculated for the parameters deduced from the

experiment (all in eV): $U = 3.1$, $J_H = 0.6$, $\Delta_{\text{JT}} = 0.7$, and $t = 0.41$. In addition, the value of $J_t = 1.67$ meV was chosen to reproduce the experimental values of J_{ab} and J_c . This value is consistent with original estimate of $J_t = 2.1$ meV deduced in Ref. 5 from the Néel temperature of CaMnO_3 , and fits remarkably well to a later estimate,⁶ $J_t \simeq 4 \times 10^{-4} t \simeq 1.64$ meV. In view of uncertainties associated with J_t and the optical excitation energies $E_1 - E_5$ entering Eqs. (12) and (13), as well as the error associated with the experimentally determined magnetic exchange parameters,³⁹ the agreement between the orbital angle determined in this analysis and the one extracted from the optical spectral weight above should be regarded as quite satisfactory.

We further note that an additional contribution to the superexchange could be associated with the $e_g \rightleftharpoons t_{2g}$ charge excitations, which would also affect the above estimate of the orbital angle θ . Indeed, according to the Tanabe-Sugano diagram⁴⁰ for the high-spin d^5 complexes, in the case of a weak ligand field ($10Dq \simeq 1.5$ eV), the LS transitions to 4T_1 and 4T_2 states lie at slightly lower energies than the LS $e_g \rightleftharpoons e_g$ 4A_1 transition. According to our assignment the (ii) 4A_1 transition appears at ~ 4.4 eV. Then, provided it is scaled following the d^5 Tanabe-Sugano diagram, the 4T_1 transition should appear at ~ 3.8 eV. Figures 2 and 4 show temperature changes of LS character in the b -axis spectra $\varepsilon^b(\nu)$ and $\Delta\varepsilon^b(\nu)$ around 3.8 eV, which could be associated with the $e_g \rightleftharpoons t_{2g}$ 4T_1 (and close to it 4T_2) LS states. In the b -axis response the optical band at around 3.8 eV is the first high-energy LS excitation, adjacent to the HS (i) 6A_1 low-energy excitation at 2 eV. Therefore, the isobestic point, namely the crossing point for the different temperature scans, which balances the SW transfer between the HS and LS states, appears at ~ 2.7 eV in the b -axis response.

IV. SUMMARY AND CONCLUSIONS

Several contributions can be distinguished in the optical response of LaMnO_3 crystals in the investigated spectral range: (i) charge-transfer $p - d$ transitions from the occupied O $2p$ band into the partially occupied Mn $3d$ levels, (ii) *intrasite* $d - d$ transitions between the Jahn-Teller splitted e_g levels and from the occupied t_{2g} levels into the empty e_g levels, and (iii) *intersite* $d_i - d_j$ transitions $d_i^4 d_j^1 \rightleftharpoons d_i^3 d_j^2$ (along a bond $\langle ij \rangle$) within the e_g and t_{2g} manifolds and between the t_{2g} and e_g local states. Based on a comparison to optical data on other transition metal oxides and to a variety of theoretical calculations,^{13,28,29} the pronounced optical band at 4.7 eV can be assigned to a strongly dipole-allowed O $2p - \text{Mn } 3d$ transition. An assignment of the low-energy band at 2 eV has, however, been controversial in the literature, where different possibilities from (i)-(iii) are considered.

The present ellipsometry study on the untwinned LaMnO_3 crystal clearly demonstrates that the

anisotropic optical SWs in the energy window covered by our experiment are strongly influenced by the onset of long-range antiferromagnetic order at T_N . Since both (i) the charge-transfer excitations between the O $2p$ and Mn $3d$ orbitals and (ii) the intrasite $d-d$ transitions should not be affected by the relative orientation of neighboring Mn spins (near the magnetic transition), we associate strongly T -dependent bands with (iii) the intersite d_i-d_j transitions. We discovered that the onset of long-range antiferromagnetic order causes critical SW redistribution around the Néel temperature T_N between the low- and high-energy counterparts, located around 2 and 5 eV, which we associate with parallel (HS) and antiparallel (LS) spin transfer between the neighboring ions. The experimentally determined temperature variations of the anisotropic optical SW of the low-energy optical band at 2 eV (HS part) are in a good quantitative agreement with the superexchange model that attributes them to the temperature-dependent spin correlations between Mn spins. This interpretation was possible as the energy scales of spin and orbital interactions are well separated from each other in LaMnO_3 , i.e. $T_N \ll T_{\text{OO}}$, and therefore only the onset of the spin order influences the distribution of SWs in the relevant regime of temperature, while the orbital order is practically unchanged.³⁶

From the anisotropy ratio of the low- and high-temperature SW of the 2 eV HS-state excitation we obtain a reasonable estimate for the orbital angle θ , consistent with the structural data.²⁵ The LS higher-energy counterpart appears in our spectra on a broad-band background of the strongly dipole-allowed O $2p$ - Mn $3d$ charge-transfer transition located at around $\Delta \simeq 4.7$ eV. Nonetheless, using a careful study of the temperature dependencies in combination with a dispersion analysis, we were able to separate LS-state transitions. The description of the multiplet structure in the framework of the intersite $d_i^4 d_j^4 \rightleftharpoons d_i^3 d_j^5$ transitions by the e_g electrons, based on the d^5 Tanabe-Sugano diagram,⁴⁰ allowed us to evaluate the effective parameters: $U \simeq 3.1$ eV, $J_H \simeq 0.6$ eV, and $\Delta_{\text{JT}} \simeq 0.7$ eV, while the value of $t \simeq 0.41$ eV was deduced from the overall redistribution of the SW due to the onset of the magnetic order.

Finally, we emphasize that the overall consistent pic-

ture of the optical spectra and magnetic properties deduced from the present study confirms that the lowest-energy optical excitation at around 2 eV has the d_i-d_j origin and is associated with Mott-Hubbard excitations, while the strongly-dipole allowed $p-d$ CT transition emerges at a higher energy around 4.7 eV. The latter observation is in reasonable agreement with the optical excitation energy of the CT transition $\text{Mn}^{3+} + \text{O}^{2-} \rightarrow \text{Mn}^{2+} + \text{O}^-$ calculated at $E_{\text{opt}} \simeq 5.6$ eV in the shell model approximation,²⁸ which takes into account environmental factors (covalency, polarization, *etc.*), important in many oxide systems⁴¹. As we discussed, such effects are responsible for the considerable reduction of the local Coulomb interaction from the respective bare value. However, we note that the 2 eV peak, assigned to the d_i-d_j transition in this study, is observed at a lower energy than that estimated in Ref. 28 for the energy of the intersite transition $\text{Mn}^{3+} + \text{Mn}^{3+} \rightarrow \text{Mn}^{2+} + \text{Mn}^{4+}$ at $E_{\text{opt}} \simeq 3.7$ eV. More elaborate theoretical and experimental study is required to elucidate the origin of this discrepancy, to understand the three-subband structure of the lowest-energy optical band, and to verify the value of the on-site Coulomb interaction U .

Summarizing, the above analysis implies that LaMnO_3 is in the regime of a Mott-Hubbard rather than charge transfer system according to the original classification of Zaanen, Sawatzky and Allen. Whether the insulating ground state of LaMnO_3 follows primarily from strong electronic correlations, or is due to strong lattice distortions, is still under debate at present.

Acknowledgments

We thank D. Khomskii, F. V. Kusmartsev, A. V. Boris and A. M. Stoneham for fruitful discussions. We also thank M. Salman for the participation in the ellipsometry measurements, A. Kulakov for detwinning of the crystal, J. Stempfer, I. Zegkinoglou, and M. Schulz for the characterization of the crystal. A.M.O. acknowledges financial support by the Foundation for Polish Science (FNP) and by the Polish Ministry of Science and Higher Education under Project No. N202 068 32/1481.

¹ J. B. Goodenough, Phys. Rev. **100**, 564 (1955); M. D. Kaplan and B. C. Vekhter, *Cooperative phenomena in Jahn-Teller crystals* (Plenum, New York, 1995); E. Dagotto, T. Hotta, and A. Moreo, Phys. Rep. **344**, 1 (2001).

² J. Kanamori, J. Appl. Phys. **31**, S14 (1960).

³ A. Yamasaki, M. Feldbacher, Y.-F. Yang, O. K. Andersen, and K. Held, Phys. Rev. Lett. **96**, 166401 (2006). Y.-F. Yang and K. Held, Phys. Rev. B **76**, 212401 (2007).

⁴ K. I. Kugel and D. I. Khomskii, Sov. Phys. Usp. **25**, 231 (1982).

⁵ L. F. Feiner and A. M. Oleś, Phys. Rev. B **59**, 3295 (1999).

⁶ A. M. Oleś, G. Khaliullin, P. Horsch, and L. F. Feiner, Phys. Rev. B **72**, 214431 (2005).

⁷ G. Khaliullin, Prog. Theor. Phys. Suppl. **160**, 155 (2005).

⁸ P. Benedetti and R. Zeyher, Phys. Rev. B **59**, 9923 (1999).

⁹ Y. Tokura and N. Nagaosa, Science **288**, 462 (2000).

¹⁰ K. H. Ahn and A. J. Millis, Phys. Rev. B **61**, 13545 (2000).

¹¹ C. Ederer, C. Lin, and A. J. Millis, Phys. Rev. B **76**, 155105 (2007); C. Lin and A. J. Millis, *ibid.* **78**, 174419 (2008).

¹² J. Zaanen, G. A. Sawatzky, and J. W. Allen, Phys. Rev. Lett. **55**, 418 (1985).

- ¹³ T. Arima and Y. Tokura, J. Phys. Soc. Jpn. **64**, 2488 (1995); T. Arima, Y. Tokura, and J. B. Torrance, Phys. Rev. B **48**, 17006 (1993).
- ¹⁴ J. Zaanen and A. M. Oleś, Phys. Rev. B **48**, 7197 (1993).
- ¹⁵ S. Piskunov, E. Spohr, T. Jacob, E. Kotomin, D. Ellis, Phys. Rev. B **76**, 012410 (2007).
- ¹⁶ E. A. Kotomin, R. A. Evarestov, Yu. A. Maistrikov, J. Maier, Phys. Chem. Chem. Phys. **7**, 2346 (2005).
- ¹⁷ K. Tobe, K. Kimura, Y. Okimoto, and Y. Tokura, Phys. Rev. B **64**, 184421 (2001).
- ¹⁸ M. A. Quijada, J. R. Simpson, L. Vasiliu-Doloc, J. W. Lynn, H. D. Drew, Y. M. Mukovskii, and S. G. Karabashchev, Phys. Rev. B **64**, 224426 (2001).
- ¹⁹ N. N. Kovaleva, A. V. Boris, C. Bernhard, A. Kulakov, A. Pimenov, A. M. Balbashov, G. Khaliullin, and B. Keimer, Phys. Rev. Lett. **93** 147204 (2004).
- ²⁰ S. Miyasaka, Y. Okimoto, and Y. Tokura, J. Phys. Soc. Jpn. **71**, 2086 (2002).
- ²¹ A. A. Tsvetkov, F. P. Mena, P. H. M. van Loosdrecht, D. van der Marel, Y. Ren, A. A. Nugroho, A. A. Menovsky, I. S. Elfimov, and G. A. Sawatzky, Phys. Rev. B **69**, 075110 (2004).
- ²² J. S. Lee, Y. S. Lee, T. W. Noh, S.-J. Oh, Jaejun Yu, S. Nakatsuji, H. Fukazawa, and Y. Maeno, Phys. Rev. Lett. **89**, 257402 (2002).
- ²³ N. N. Kovaleva, A. V. Boris, P. Yordanov, A. Maljuk, E. Brücher, J. Stremper, M. Konuma, I. Zegkinoglou, C. Bernhard, A. M. Stoneham, and B. Keimer, Phys. Rev. B **76**, 155125 (2007).
- ²⁴ G. Khaliullin, P. Horsch, and A. M. Oleś, Phys. Rev. B **70**, 195103 (2004).
- ²⁵ J. Rodríguez-Carvajal, M. Hennion, F. Moussa, A. H. Moudden, L. Pinsard, and A. Revcolevschi, Phys. Rev. B **57**, R3189 (1998).
- ²⁶ A. M. Balbashov, S. G. Karabashchev, Ya. M. Mukovskiy, and S. A. Zverkov, J. Cryst. Growth **167**, 365 (1996); A. M. Balbashov and S. K. Egorov, J. Cryst. Growth **52**, 498 (1981).
- ²⁷ J. Kircher, J. Humlíček, M. Garriga, M. Cardona, D. Fuchs, H.-U. Habermeier, O. Jepsen, S. Gopalan, O. K. Andersen, Y. Fang, U. Welp, K. G. Vandervoort, and G. W. Crabtree, Physica C **192**, 473 (1992).
- ²⁸ N. N. Kovaleva, J. L. Gavartin, A. L. Shluger, A. V. Boris, and A. M. Stoneham, J. Exp. Theor. Phys. **94**, 178 (2002); N. N. Kovaleva, J. L. Gavartin, A. L. Shluger, A. V. Boris, and A. M. Stoneham, Physica B **312-313**, 734 (2002); N. N. Kovaleva, J. L. Gavartin, A. V. Boris, and A. M. Stoneham, Physica B **312-313**, 737 (2002).
- ²⁹ A. S. Moskvina, Phys. Rev. B **65**, 205113 (2002).
- ³⁰ J. van den Brink, M. B. J. Meinders, J. Lorenzana, R. Eder, and G. A. Sawatzky, Phys. Rev. Lett. **75**, 4658 (1995); M. B. J. Meinders, J. van den Brink, J. Lorenzana, and G. A. Sawatzky, Phys. Rev. B **52**, 2484 (1995).
- ³¹ D. Baeriswyl, J. Carmelo, and A. Luther, Phys. Rev. B **33**, 7247 (1986); A. Aichhorn, P. Horsch, W. von der Linden, and M. Cuoco, *ibid.* **65**, 201101 (2002).
- ³² J. S. Griffith, *The Theory of Transition-Metal Ions* (Cambridge University Press, Cambridge, 1961).
- ³³ J. Zaanen and G. A. Sawatzky, J. Solid State Chem. **88**, 8 (1990).
- ³⁴ The present value $J_H = 0.6$ eV is consistent with that obtained in Ref. 19, where a different definition of J_H was used. The derived estimate suggests a considerable screening of the atomic value³³ of $J_H \simeq 0.9$ eV deduced from the Racah parameters B and C , see Ref. 33.
- ³⁵ As explained in the text, the effective parameter U is reduced from the intraorbital Coulomb interaction due to excitonic and polarization effects³⁰ that accompany intersite optical transitions. The value of U deduced from the photoemission experiments, see A. E. Bocquet, T. Mizokawa, T. Saitoh, H. Namatame, and A. Fujimori, Phys. Rev. B **46**, 3771 (1992), or used in recent electronic structure calculations for LaMnO_3 ³ is ~ 5 eV.
- ³⁶ The orbital angle θ may change somewhat near the magnetic transition at T_N as the balance between the superexchange and the effective orbital interactions induced by the lattice distortions changes; this effect was ignored in the present analysis.
- ³⁷ The same value of $t \simeq 0.41$ eV was estimated also from the CT model,⁵ and provides a satisfactory description of the magnon excitation spectra in the ferromagnetic metallic manganites, see G. Khaliullin and R. Kilian, Phys. Rev. B **61**, 3494 (2000); A. M. Oleś and L. F. Feiner, *ibid.* **65**, 052414 (2002).
- ³⁸ Note that a rather small finite weight would result from quantum fluctuations in the A -type antiferromagnetic phase, see M. Raczkowski and A. M. Oleś, Phys. Rev. B **66**, 094431 (2002).
- ³⁹ K. Hirota, N. Kaneko, A. Nishizawa, and Y. Endoh, J. Phys. Soc. Jpn. **65**, 3736 (1996); F. Moussa, M. Hennion, J. Rodríguez-Carvajal, H. Moudden, L. Pinsard, and A. Revcolevschi, Phys. Rev. B **54**, 15149 (1996); G. Biotteau, M. Hennion, F. Moussa, J. Rodríguez-Carvajal, L. Pinsard, A. Revcolevschi, Y. M. Mukovskii, and D. Shulyatev, *ibid.* **64**, 104421 (2001).
- ⁴⁰ S. Sugano, Y. Tanabe, and H. Kamimura, *Multiplets of Transition-Metal Ions in Crystals* (Academic Press, New York, 1970).
- ⁴¹ A. M. Stoneham and M. J. L. Sangster, Phil. Mag. B **43**, 609 (1980).

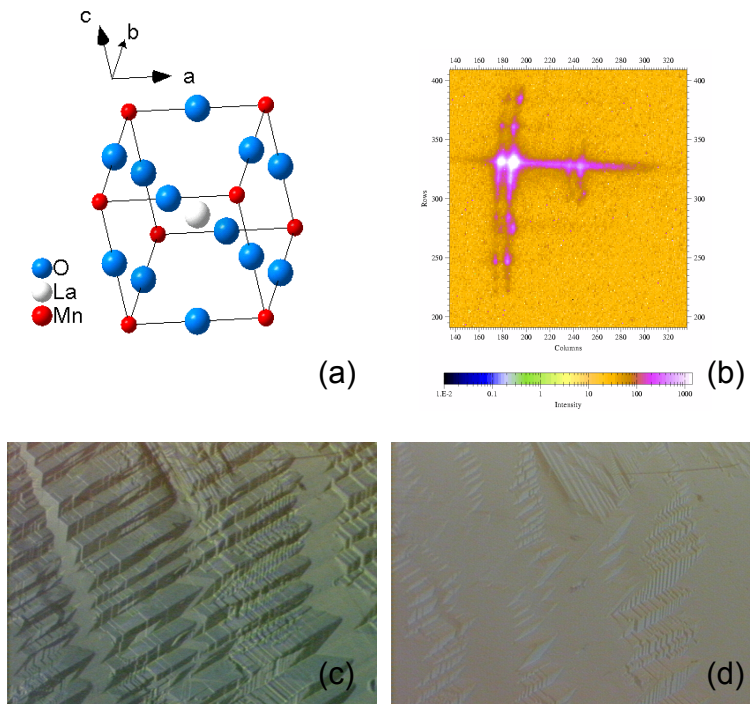


FIG. 1: (Color) (a) Pseudocubic perovskite structure of LaMnO_3 (space group $Pm\bar{3}m$) above $T_{OO} \simeq 780$ K. Room temperature polarized optical images showing a part of the LaMnO_3 crystal (of $200 \mu\text{m}$ length) (c) initially heavily twinned and (d) after detwinning; (b) Laue diagram demonstrating 95 % detwinning at a particular surface location.

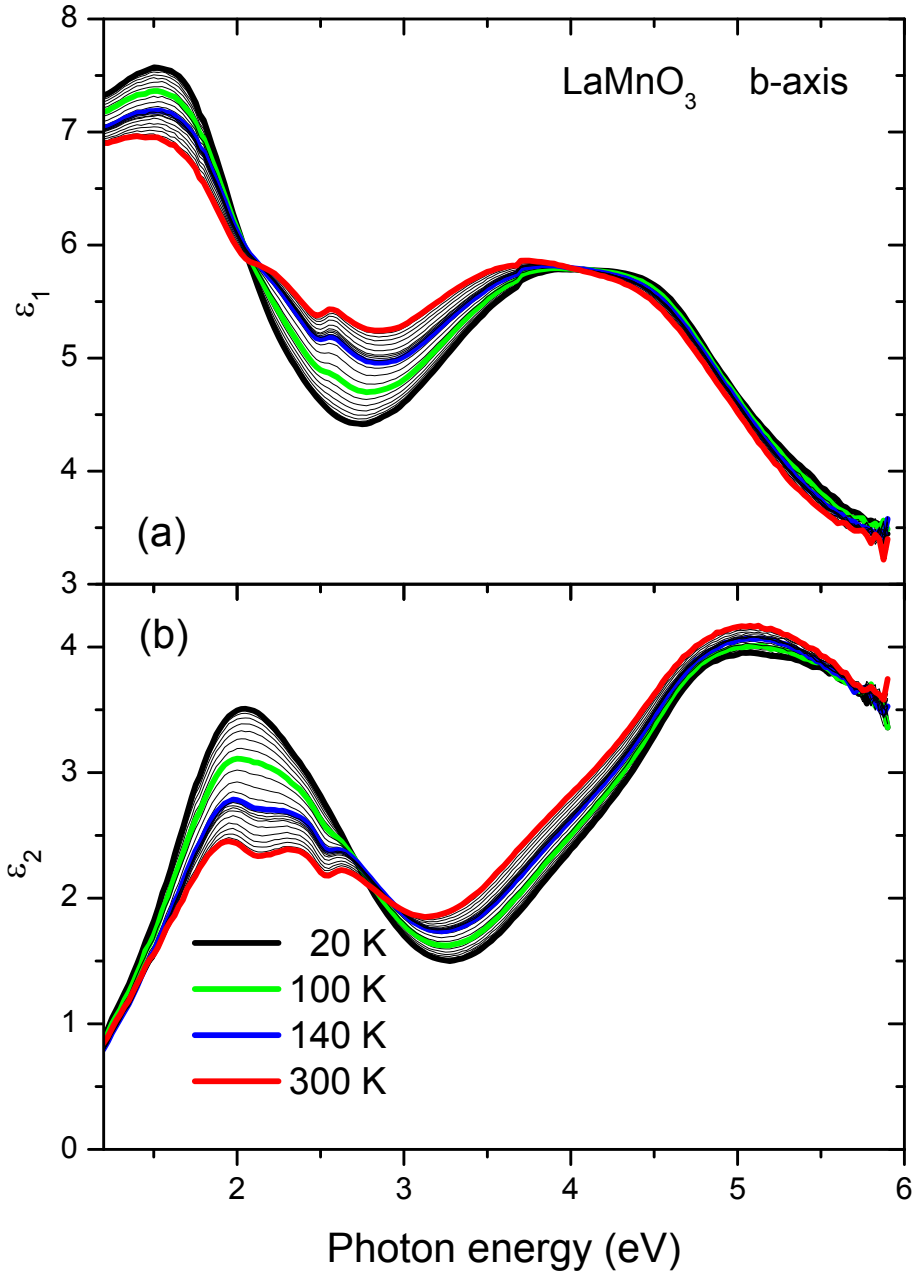


FIG. 2: (Color online) Temperature variation of the (a) real $\varepsilon_1(\nu)$ and (b) imaginary $\varepsilon_2(\nu)$ parts of the complex dielectric function spectra of the untwinned LaMnO₃ crystal in b -axis polarization. The representative spectra at the temperatures around $T_N \simeq 140$ K are indicated. The temperature evolution of the spectra (here and in the following figures) is shown in successive temperature intervals of 10 K between 20 and 200 K and of 25 K between 200 and 300 K.

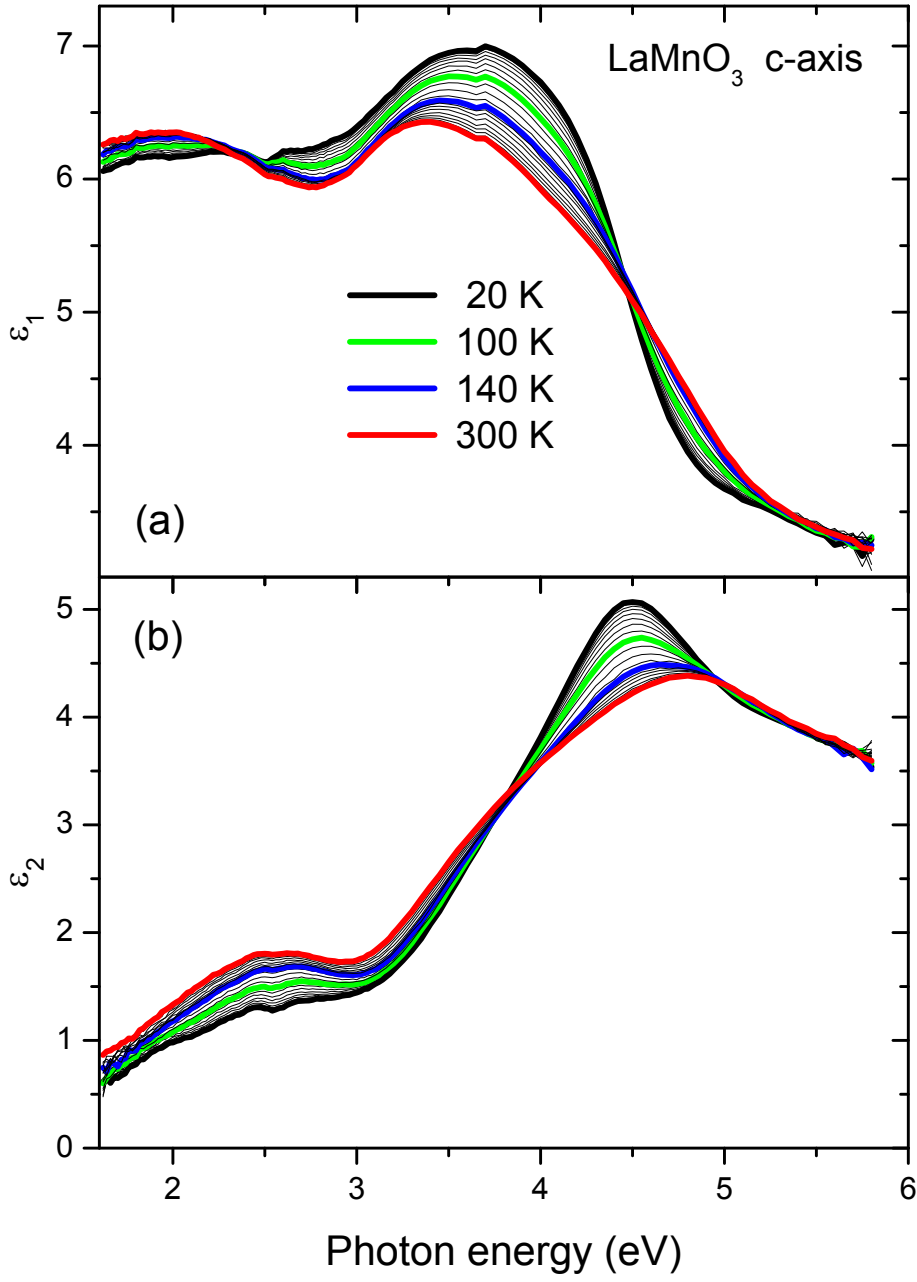


FIG. 3: (Color online) Temperature variation of the (a) real $\epsilon_1(\nu)$ and (b) imaginary $\epsilon_2(\nu)$ parts of the complex dielectric function spectra of the untwinned LaMnO₃ crystal in *c*-axis polarization.

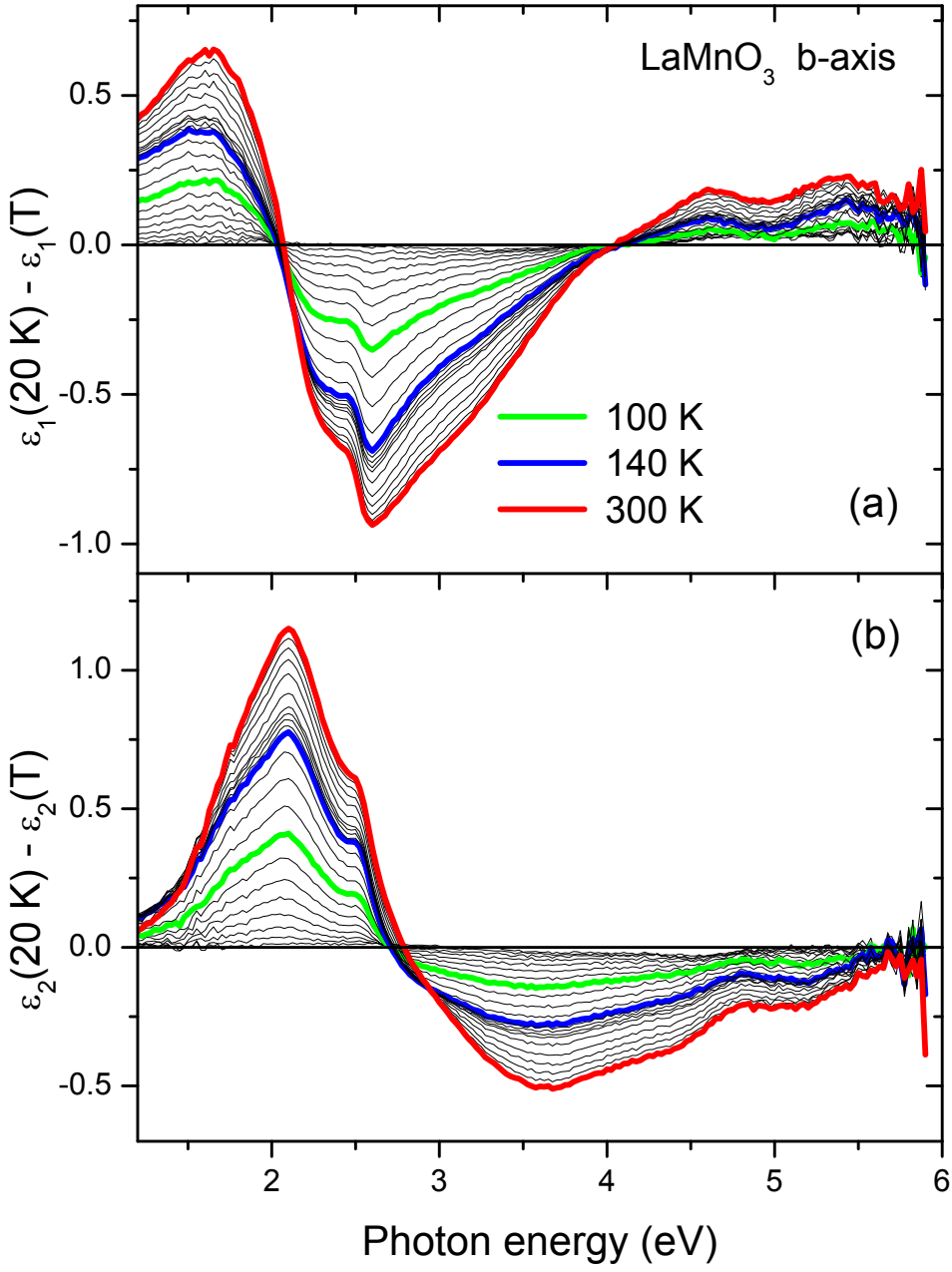


FIG. 4: (Color online) Temperature variation of the (a) real $\Delta\varepsilon_1(20K, T) = \varepsilon_1(\nu, 20K) - \varepsilon_1(\nu, T)$ and (b) imaginary $\Delta\varepsilon_2(20K, T) = \varepsilon_2(\nu, 20K) - \varepsilon_2(\nu, T)$ parts of the difference between the low-temperature complex dielectric function spectra measured at 20 K and the corresponding T -dependent spectra in the b -axis polarization.

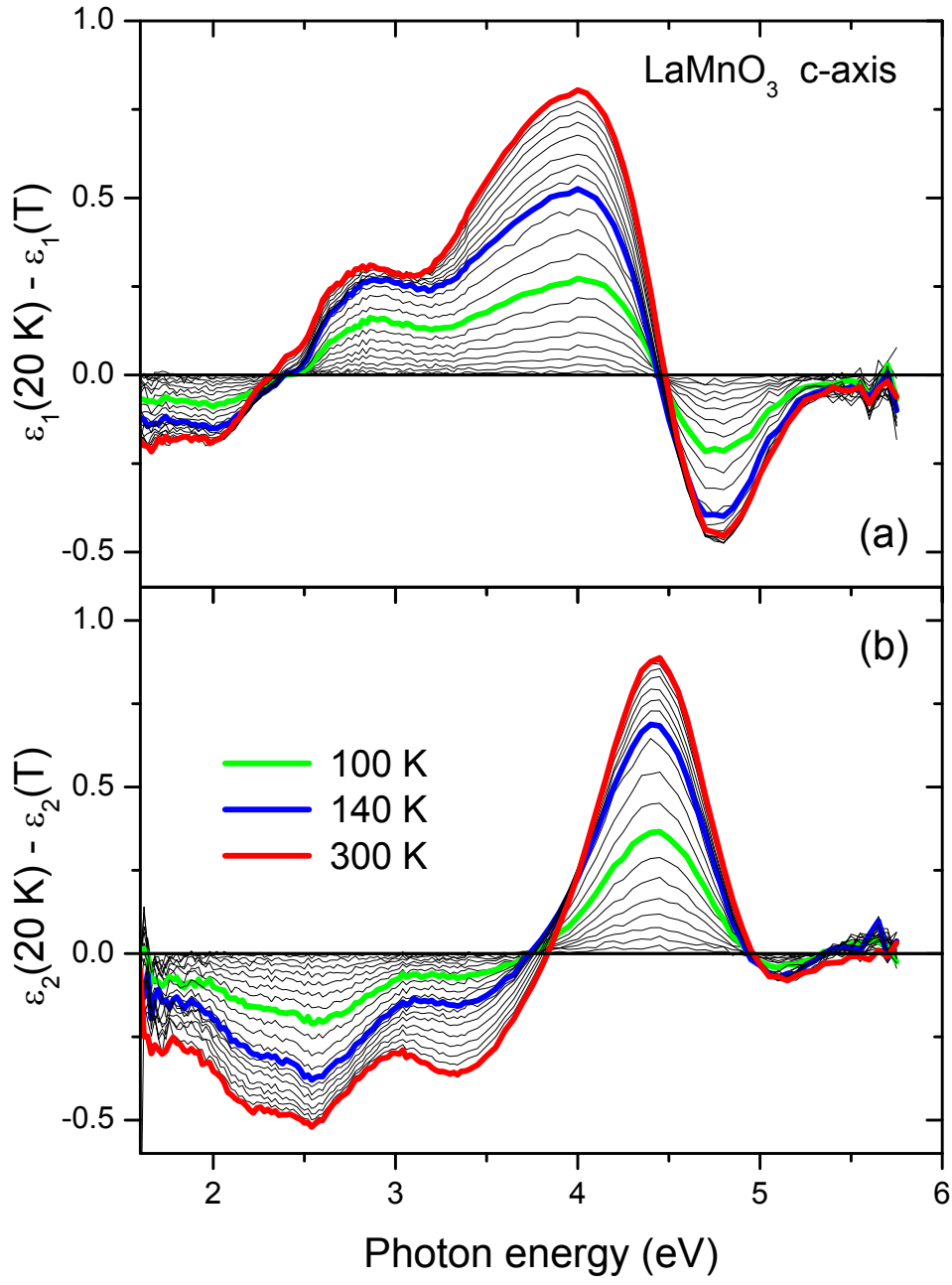


FIG. 5: (Color online) Temperature variation of the difference of the (a) real part $\Delta\varepsilon_1(20K, T) = \varepsilon_1(\nu, 20K) - \varepsilon_1(\nu, T)$, and (b) imaginary part $\Delta\varepsilon_2(20K, T) = \varepsilon_2(\nu, 20K) - \varepsilon_2(\nu, T)$ of the dielectric response in the c -axis polarization.

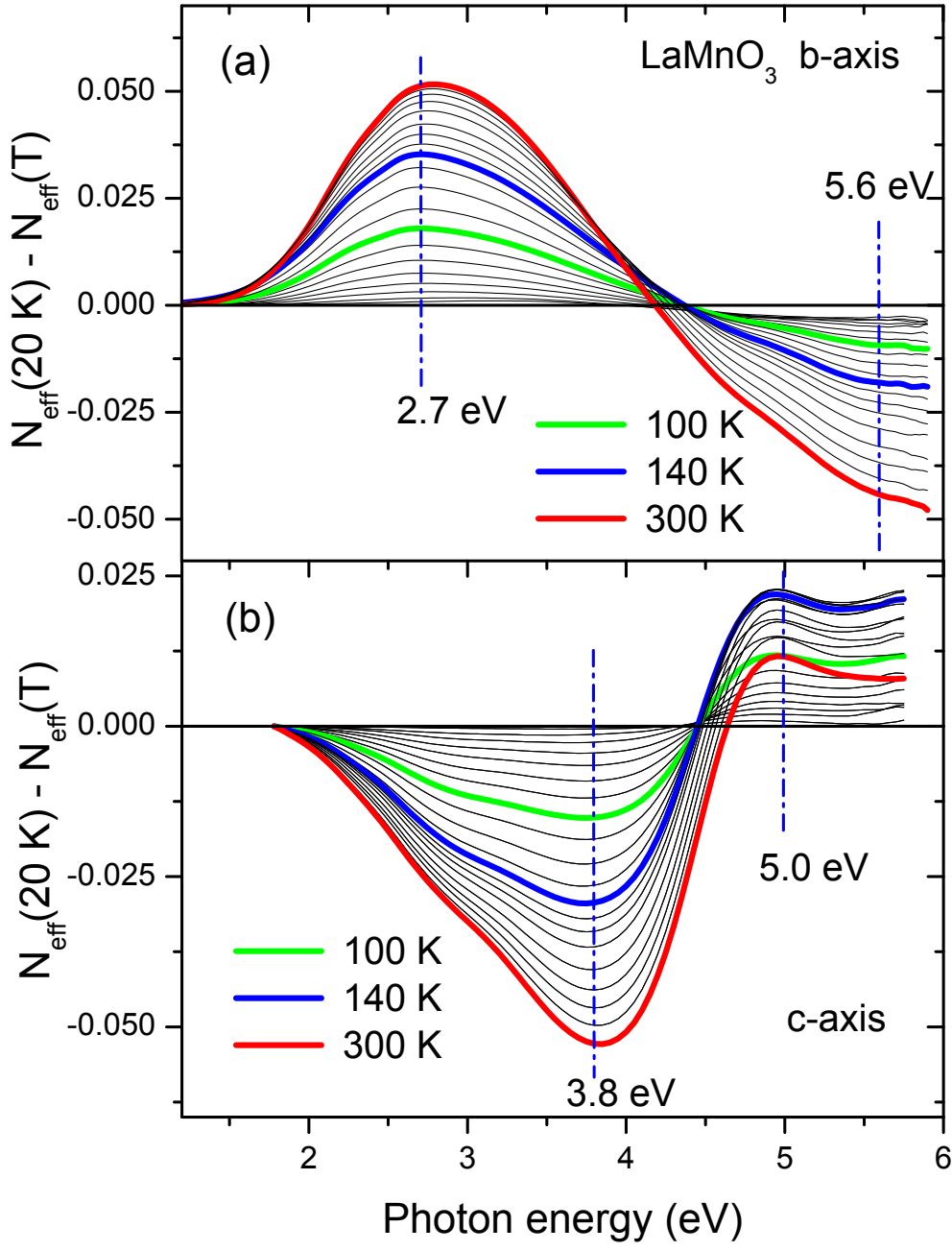


FIG. 6: (Color online) Spectral and temperature dependencies of the SW shifts $\Delta N_{\text{eff}}(20\text{K}, T) = N_{\text{eff}}(20\text{K}) - N_{\text{eff}}(T)$ in the (a) *b*-axis and (b) *c*-axis polarization.

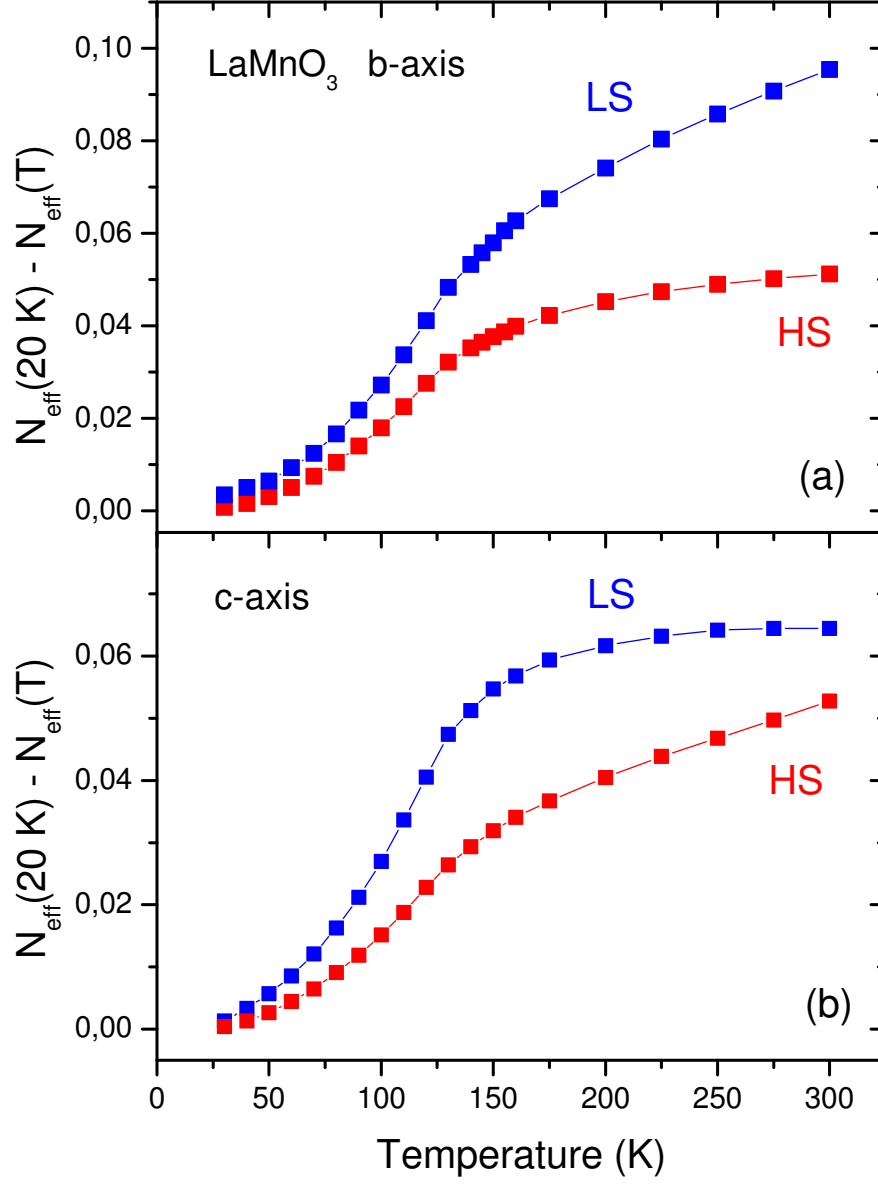


FIG. 7: (Color online) *Partial SW gain or loss* of the low- and high-energy optical bands in the (a) *b*-axis $\Delta N_{\text{eff},HS}^{(b)} = \frac{2m}{\pi e^2 N} \int_{1.2\text{eV}}^{2.7\text{eV}} \Delta\sigma_1(\nu', \Delta T) d\nu'$ and $\Delta N_{\text{eff},LS}^{(b)} = -\frac{2m}{\pi e^2 N} \int_{2.7\text{eV}}^{5.6\text{eV}} \Delta\sigma_1(\nu', \Delta T) d\nu'$ and (b) *c*-axis $\Delta N_{\text{eff},HS}^{(c)} = -\frac{2m}{\pi e^2 N} \int_{1.7\text{eV}}^{3.8\text{eV}} \Delta\sigma_1(\nu', \Delta T) d\nu'$ and $\Delta N_{\text{eff},LS}^{(c)} = \frac{2m}{\pi e^2 N} \int_{3.8\text{eV}}^{5.0\text{eV}} \Delta\sigma_1(\nu', \Delta T) d\nu'$.

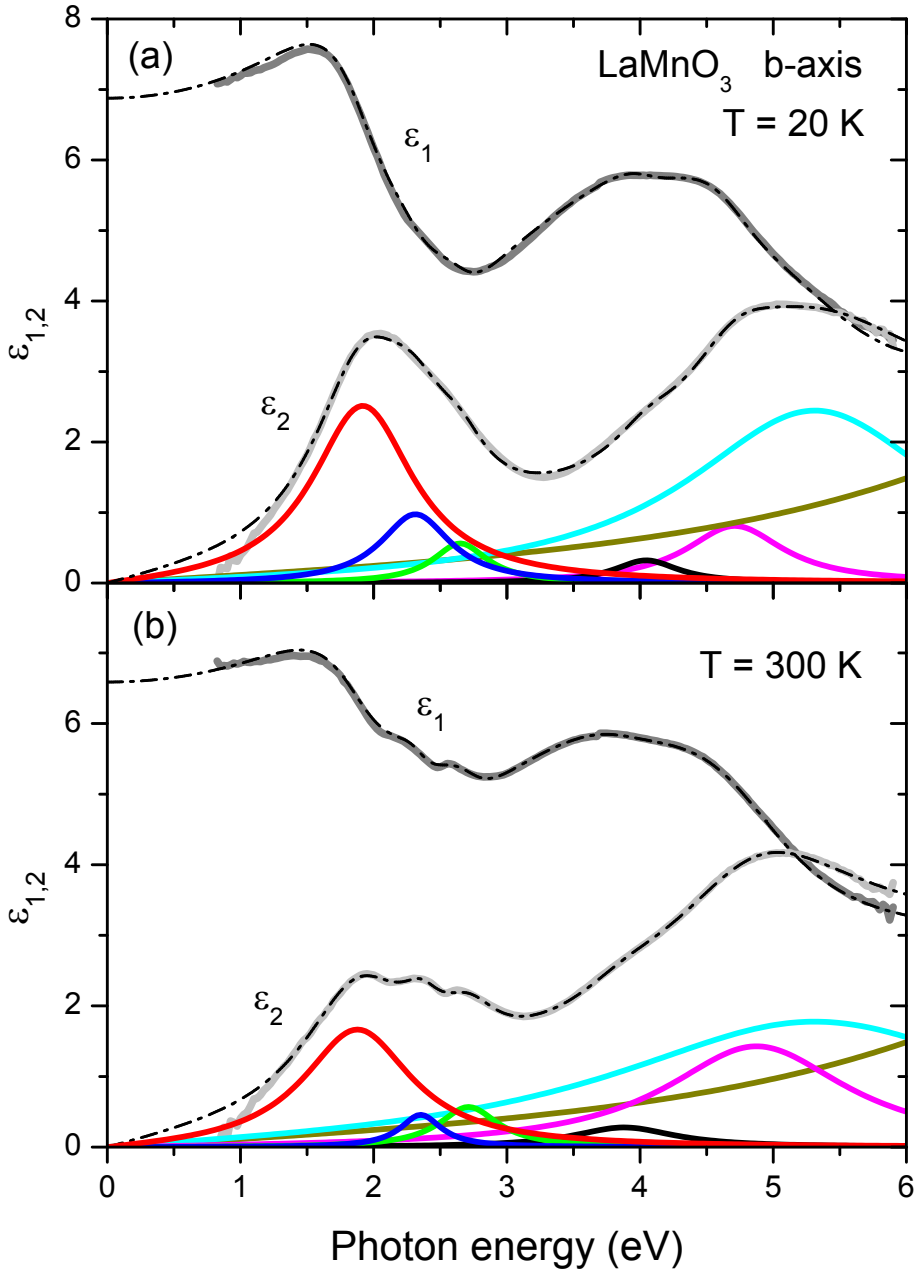


FIG. 8: (Color online) Real and imaginary part of b -axis complex dielectric response $\epsilon^b(\nu)$ at (a) 20 K and (b) 300 K, represented by the total contribution of the separate Lorentzian bands determined by the dispersion analysis, as described in the text.

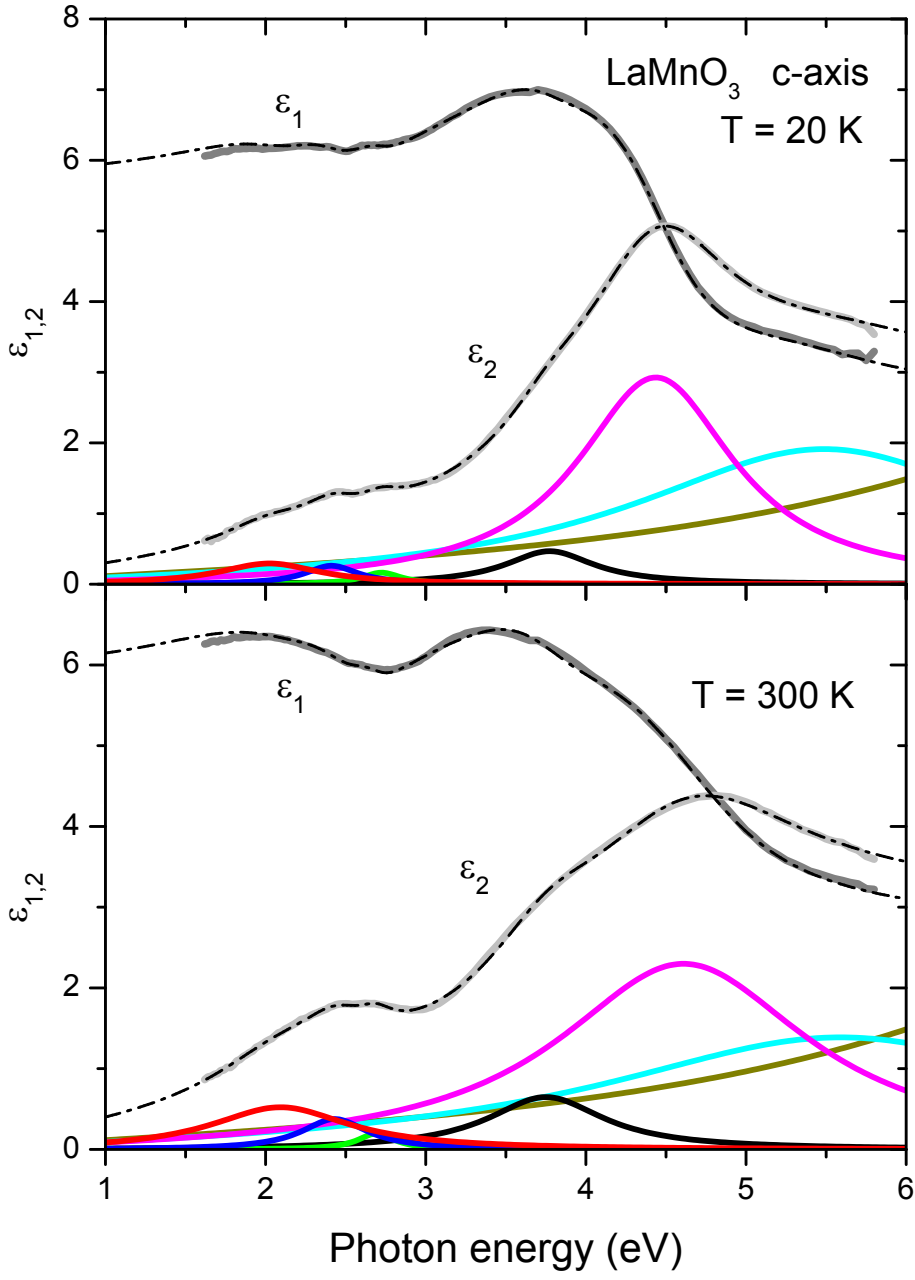


FIG. 9: (Color online) Real and imaginary part of c -axis complex dielectric response $\tilde{\epsilon}^c(\nu)$ at (a) 20 K and (b) 300 K, represented by the total contribution of the separate Lorentzian bands determined by the dispersion analysis.

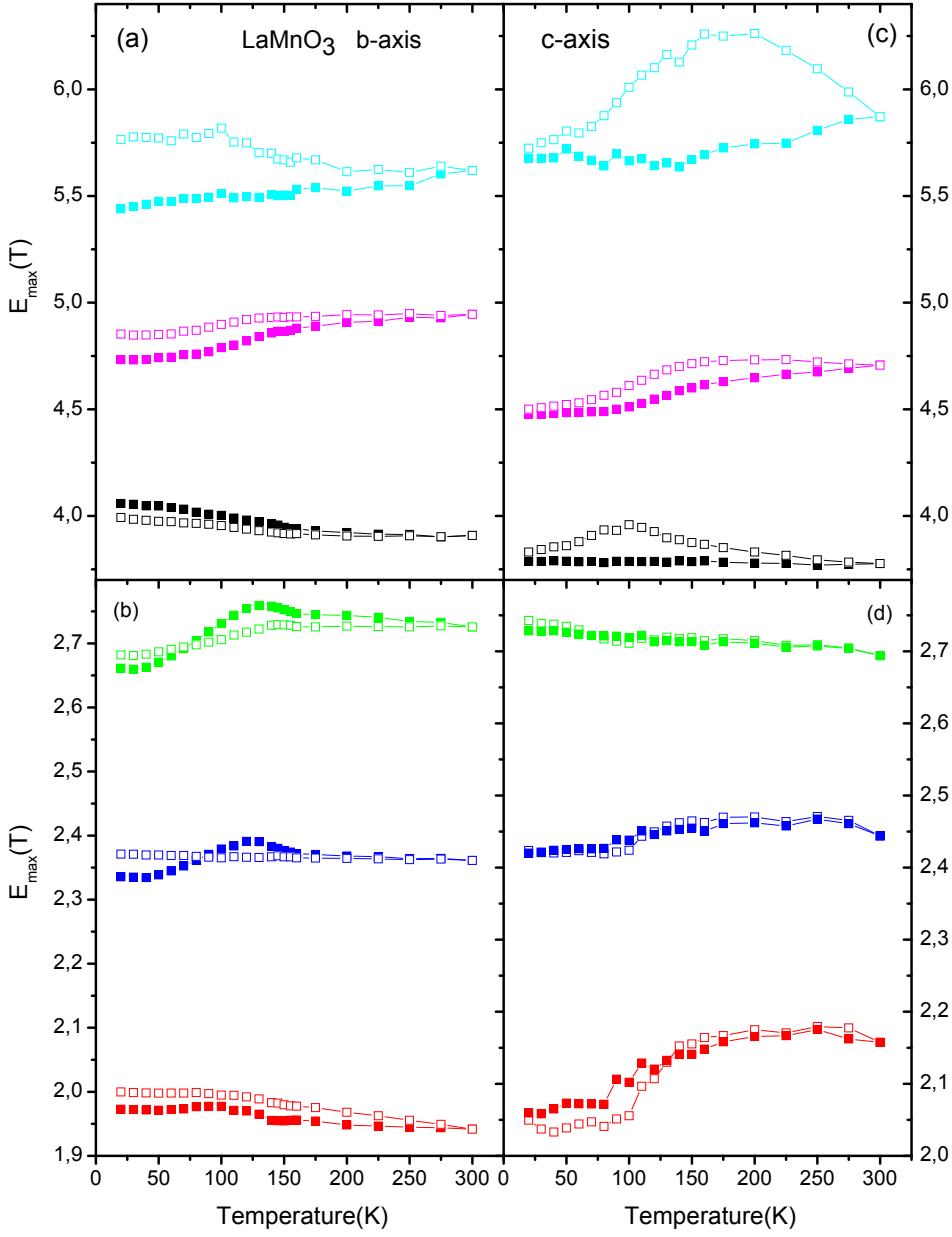


FIG. 10: (Color online) Temperature dependencies of the peak energies ν_j in the spectral ranges of the low- and high-energy optical bands, as determined by the dispersion analysis, in the (a) and (b) *b*-axis and (c) and (d) *c*-axis polarization. The filled symbols show the results of the fit from 20 to 300 K, the open symbols show the results of the fit from 300 to 20 K.

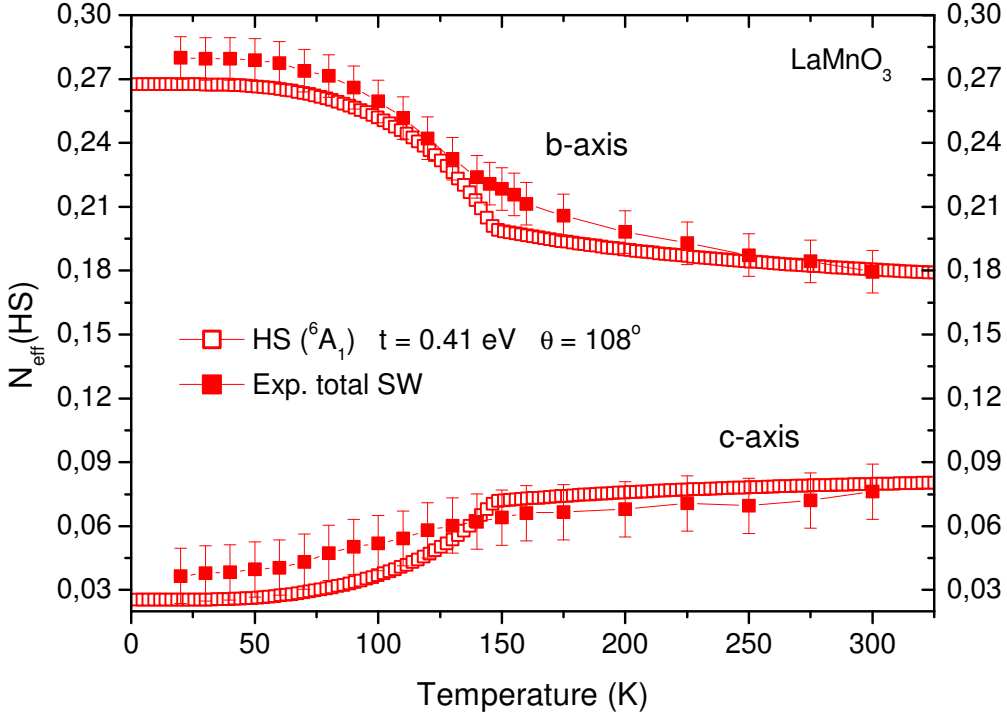


FIG. 11: (Color online) Temperature and polarization dependencies of the *total* SW N_{eff} of the low-energy optical band, represented by a summary contribution from the three Lorentzian subbands (the temperature dependencies of the subbands are detailed in Ref. 19).

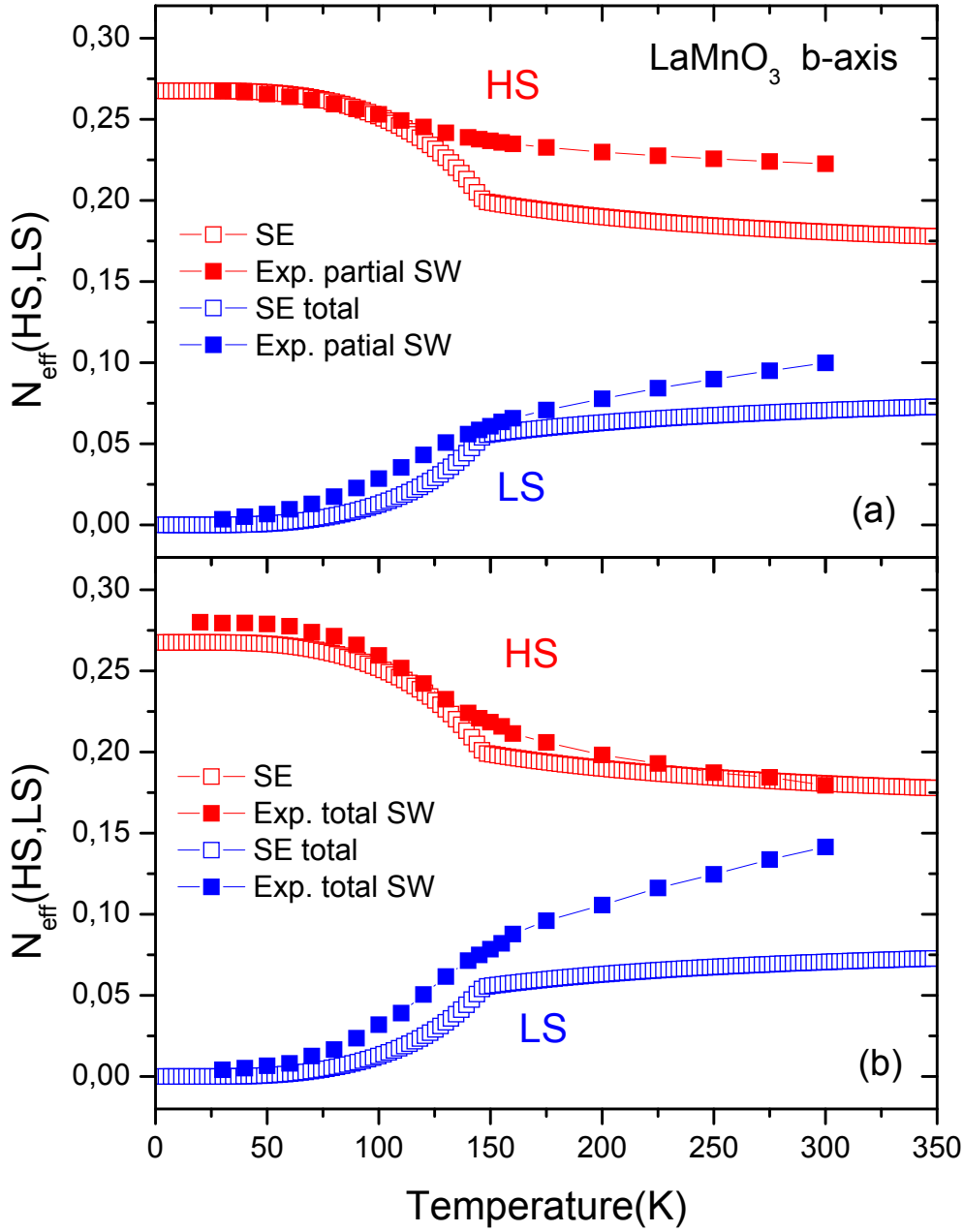


FIG. 12: (Color online) Comparison between the experimental (a) *partial* and (b) *total* (filled symbols) and the calculated (*total*) (empty symbols) SW for the HS- and LS- optical bands in the *b*-axis polarization.

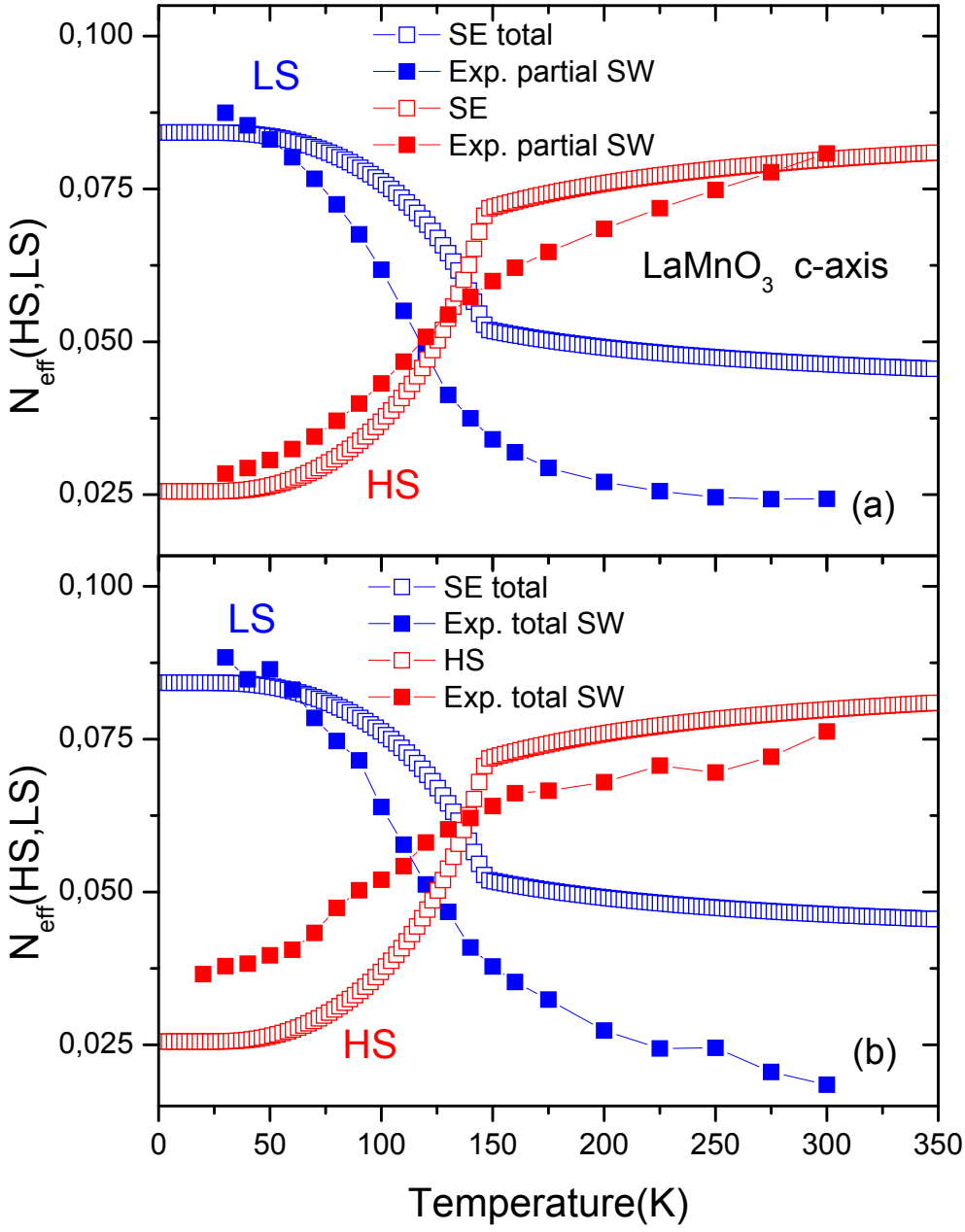


FIG. 13: (Color online) Comparison between the experimental (a) *partial* and (b) *total* (filled symbols) and the calculated (*total*) (empty symbols) SW for the HS- and LS- optical bands in the *c*-axis polarization.

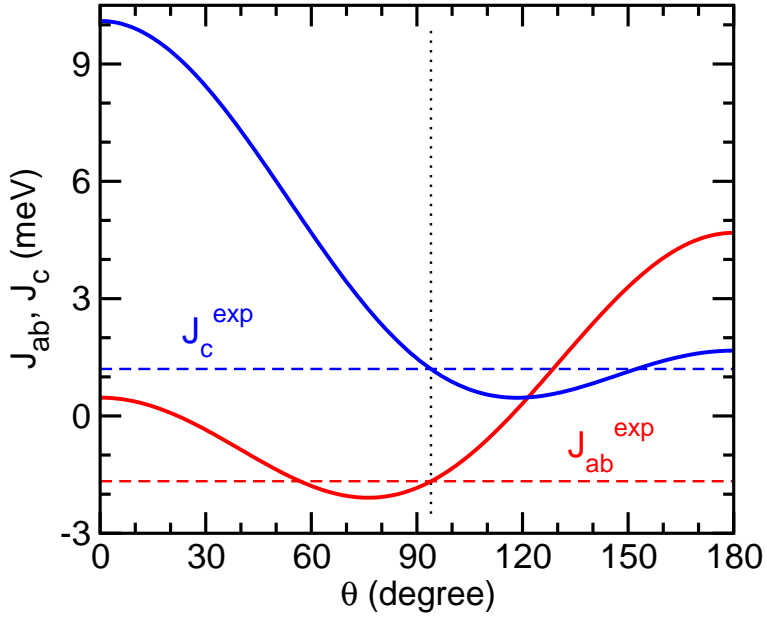


FIG. 14: (Color online) Magnetic exchange constants, J_{ab} and J_c , as obtained for the varying orbital angle θ from Eqs. (12) and (13). Parameters: $U = 3.1$ eV, $J_H = 0.6$ eV, $\Delta_{JT} = 0.7$ eV, $t = 0.41$ eV, and $J_t = 1.67$ meV. Dashed lines indicate the experimental values of J_{ab} and J_c determined by neutron scattering³⁹ in LaMnO_3 .